A computational framework for crack propagation along contact interfaces and surfaces under load

Ignatios Athanasiadis[a], Andrei G. Shvarts[a], Zahur Ullah[a,b], Karol Lewandowski[a],
Chris J. Pearce[a], Łukasz Kaczmarczyk[a,*]

[a] *Glasgow Computational Engineering Centre (GCEC), James Watt School of Engineering, University of Glasgow, Glasgow, G12 8QQ, UK*
[b] *Advanced Composites Research Group (ACRG), School of Mechanical and Aerospace Engineering, Queen's University Belfast, Belfast, BT9 5AH, UK*

Graphical Abstract

Material configuration

Spatial configuration
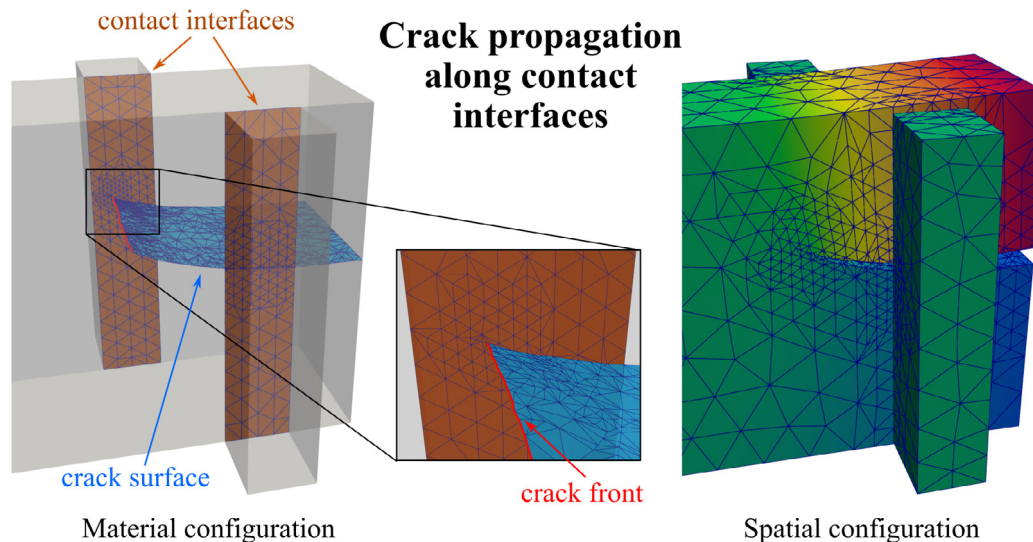
Abstract

We present the first implicit computational framework for simulating crack propagation along contact interfaces and surfaces under load in three-dimensional bodies, which is distinct from modelling the contact interaction associated with crack closure. We restrict ourselves to brittle fracture and frictionless contact and focus on numerical challenges associated with the coupling

* Corresponding author.
  E-mail addresses: ignatios.athanasiadis@glasgow.ac.uk (I. Athanasiadis), andrei.shvarts@glasgow.ac.uk (A.G. Shvarts),
z.ullah@qub.ac.uk (Z. Ullah), karol.lewandowski@glasgow.ac.uk (K. Lewandowski), chris.pearce@glasgow.ac.uk (C.J. Pearce),
lukasz.kaczmarczyk@glasgow.ac.uk (Ł. Kaczmarczyk).

of unilateral constraints emerging from the Griffith's criterion and the contact conditions. The formulation is based on the configurational mechanics framework and is solved using the finite element method. The approach utilises a monolithic Arbitrary Lagrangian–Eulerian formulation permitting simultaneous resolution of crack propagation and unilateral contact constraints. Contact is embedded in the model using the well-known mortar contact formulation. Evolving cracks are explicitly modelled as displacement discontinuities within the mesh. Heterogeneous approximation of arbitrary order is used to discretise spatial displacements, enabling hp-adaptive refinement around the crack front and the contact interfaces traversed by the crack. The result is a holistic approach which handles issues associated with thermodynamic consistency, numerical accuracy and robustness of the computational scheme. Several numerical examples are presented to verify the model formulation and implementation; they also highlight how contact pressure and load applied on surfaces traversed by cracks influence their propagation. The robustness of the approach is validated by comparison of our simulations with existing numerical results and an industrial experiment involving cracks of complex morphologies propagating along contact interfaces between multiple deformable bodies.
© 2023 The Author(s). Published by Elsevier B.V. This is an open access article under the CC BY license (http://creativecommons.org/licenses/by/4.0/).

1. Introduction

Modelling of brittle crack propagation in elastic solids is an important field of research due to its relevance for various engineering applications, from the design of lithium-ion batteries [1] to the assessment of safety–critical structures such as nuclear reactors [2,3].

Over the past decades, several methods have been proposed to model crack propagation [4]. The simplest approach is associated with node splitting [5]; however, in this case, crack morphology has pathological dependence on the mesh topology. Consequently, a number of methods were proposed to ensure the crack surface geometry objectivity. One of the prominent classes of such methods is based on the displacement approximation enrichment [6–8], often utilising the partition of unity property of finite element shape functions [9]. This class of methods can provide an accurate representation of stresses in the vicinity of the crack front by enrichment functions possessing an appropriate type of singularity. An alternative approach is associated with displacement enhancement methods, which enable displacement jump in the finite element without requiring displacement conformity [10]. This class of methods is robust in the case of complex crack morphology, however, it does not provide the accuracy offered by approximation enrichment methods.

Issues of objectivity, accuracy and robustness can be targeted by techniques directly changing mesh topology to resolve crack surface geometry, which include re-meshing or mesh cutting methods [11]. Alternatively, for materials with a large fracture process zone compared to characteristic length of a structure, the concept of cohesive elements can be used [12]. Furthermore, for such cases, methods based on fracture energy, such as the crack band method [13,14], phase field methods [15] and gradient damage methods [16,17] can be utilised. This class of methods is exceptionally robust and can handle complex crack patterns, however, it demands high mesh density in the vicinity of the crack surface. To satisfy this requirement, mesh adaptation is often employed, which may impact the efficiency of the solution scheme [18].

A separate class of methods is based on discrete models, such as discrete element method [19,20], lattice methods [21,22], or peridynamics [23]. In these techniques, the fracture is handled by breaking or softening bonds between discrete elements. However, these methods have strong benefits only for problems where the characteristic size of the spatial discretisation is much smaller than the size of the fracture process zone.

One of the most rigorous approaches to the modelling of fracture is provided by configurational mechanics, offering the means to develop a thermodynamically consistent framework. Configurational forces, which are at the centre of the present work, were initially defined in the context of material defects [24,25]. This concept was later extended to model crack propagation in brittle materials: Maugin and Trimarco [26] and Gurtin and Podio-Guidugli [27] derived equations that describe the motion of the crack driven by configurational forces. Since then, configurational forces were used to find the direction of crack propagation in hyperelastic materials [28] and to solve the crack propagation problem in a staggered way for brittle [29–32] and quasi-brittle materials [33]. Configurational-forces-driven crack propagation and the Griffith criterion were combined by Kaczmarczyk et al. [2,3] who proposed a fully implicit crack propagation framework within the Arbitrary Lagrangian–Eulerian (ALE) description of motion. In this approach, the calculation of the crack front extension in 3D bodies from first principles avoids any heuristic equations dictating crack growth and leads to a continuous resolution of evolving crack path.

Modelling of brittle crack propagation becomes more complicated in the presence of contact interaction. One such example, considered in the present work, is the crack propagation in irradiated graphite bricks in a nuclear reactor [34]. In this application, one of the main challenges is the resolution of the complex crack morphology in 3D bodies subjected to internal stresses arising from irradiation and material properties' heterogeneity. The problem is further complicated by the contact interaction between different parts of the assembly present in the reactor's core. As a result, along with other nonlinearities, the computational framework describing crack extension has to handle unilateral constraints emerging from the crack propagation and from the contact interaction.

Significant developments have been achieved in the field of computational contact mechanics, see e.g. [35], especially for approaches which use Lagrange multipliers to take into account unilateral constraints, including the augmented Lagrangian method [36] and the active set method with complementarity function [37]. The mortar method is a well established and reliable approach to model contact interaction between solids having non-matching meshes, see [38,39], while a dual base for approximating the Lagrange multiplier field was proposed in [37].

Extensive computational investigations have been conducted regarding the influence of contact between crack surfaces on crack propensity and/or propagation [40–48]. In particular, crack propagation has been modelled considering frictional and adhesive contact between crack surfaces [49–54]. Some of the most popular methods for such problems are X-FEM [55–57], cohesive elements [49], phase-field [58] and short crack correction models [59]. These models are often employed to investigate the influence of fretting fatigue on the nucleation of a crack on one side of the contact interface and its propagation towards the interior of the body. This class of problem is of great importance for the railway industry [57,60–63], as well as for the aviation industry to assess the safety of turbine blades assembly [64–66].

However, in industrial applications of quasi-static crack propagation considered in this paper, possible closure of the crack surfaces and contact between them does not have a predominant effect on the solution. At the same time, cases when the trace of the crack front is located on one of the sides of a contact interface have to be thoroughly addressed to model relevant practical cases. In such scenarios, we need a robust numerical tool to assess the influence of the contact traction on the evolving crack morphology.

There are only a few studies which consider crack propagation predominantly driven by external normal contact loading. A number of 2D models have been presented [67,68], however, the important case of crack propagation along contact interfaces cannot be studied in 2D. An explicit 3D framework has been proposed using NURBS to model frictional contact and the phase-field approach to represent fracture developing along contact interfaces [69]. Implicit staggered 3D crack propagation approaches were also presented for ductile fracture developed under contact load [70,71].

In the present paper, a 3D crack propagation framework based on the configurational mechanics and ALE formulation, initially presented for homogeneous materials [2,3] and subsequently for heterogeneous materials [72], is extended to consider crack propagation along contact interfaces and, more generally, any surfaces under traction. The key contribution of the present work is the first fully implicit framework for brittle fracture which permits simultaneous solution of two sets of unilateral constraints: those associated with crack propagation and with contact conditions, including the cases when the crack front meets a contact interface.

The main advantage of the proposed method compared to the above discussed is the combination of stability, robustness, thermodynamical consistency and absence of any heuristics and pre-determination of crack paths. Furthermore, the implicit crack propagation algorithm provides error control and can negotiate challenging geometrical features such as corners. In addition, in the developed framework adaptive hp-refinement techniques are utilised, permitting to rise approximation order in the vicinity of the crack front where the error is known *a priori* to be higher. Accordingly, the contact elements on the interface traversed by the crack front also undergo hp-refinement. Notably, higher order approximations are particularly efficient in the cases of distorted elements that can emerge from the mesh evolution in the implicit crack propagation. A possible drawback of the proposed algorithm is the complexity of its implementation, in particular, linearisation of virtual work terms in the ALE formalism. However, herein we try to describe the framework in clear and concise manner, outline the implementation and provide numerical examples which verify one "feature" of the framework at a time.

We propose a theoretical framework for analysing crack propagation within elastic bodies subject to contact conditions and quasi-static loading, valid for large deformations and large displacements. However, for the engineering applications considered in the present work, small strains and small displacements are valid assumptions. Hence, the proposed model was implemented for the case of small strains and small displacements, and all results

presented involve problems where such assumptions are valid. Moreover, for contact surfaces which are traversed by the trace of the crack front, the large underlying material displacements arising from crack extension and mesh quality improvement have been tackled by enforcing consistent integration of contact pressure on both sides of the contact interface. This can be achieved by either convecting the Gauss points on the contact interface [39], or by utilising the ALE formulation to preserve the "shadowing" of contact elements originally placed on top of each other. Such "matching-meshes" approach is a particular case of mortar contact and avoids the need of linearisation of Gauss points which leads to additional non-linearities [39]. The main consequence of the chosen approach is that it restricts the model to allow for crack propagation only on contact surfaces that have no initial gap in the reference configuration.

The rest of the article is organised as follows. Governing equations for crack propagation kinematics in the Arbitrary Lagrangian Eulerian framework, along with coupling of crack propagation with traction boundary conditions and contact interface constraints are presented in Section 2. Thereafter, the variational form of the governing equations is presented in Section 3 and its discrete form is then discussed in Section 4, paying particular attention to the cases when contact interfaces and surfaces under traction are traversed by the crack front. In Section 5 we provide the verification of mortar contact implementation with hierarchical spatially heterogeneous base functions and validation of its integration in crack propagation algorithm. Furthermore, several examples are listed to highlight the effect of the contact pressure and external traction on the crack propagation process. Finally, in the same section we present an application of the proposed framework to an industrial problem and compare simulation results to experimental data considering various modelling choices.

2. Governing equations

2.1. Crack propagation kinematics

For completeness, a detailed description of the thermodynamically-consistent brittle crack propagation framework is presented in this section. In Section 2.1.1, the ALE decomposition of cracked body motion is described and is followed by the presentation of the crack front increment analysis in Section 2.1.2. Thereafter, a brief expression regarding energy dissipation in the context of Griffith criterion is given in Section 2.2, while handling of the crack propagation constraints is discussed in Section 2.3. Finally, additional boundary conditions and contact constraints are described in Sections 2.4 and 2.5, respectively.

2.1.1. Cracked body kinematics

Analysis of continuous evolution of crack propagation in brittle materials is undertaken by means of the Arbitrary Lagrangian–Eulerian (ALE) description as presented in [2,3]. The central concept of ALE approach for crack propagation is the decomposition of the body kinematics into current material and current spatial configurations (see Fig. 1). More specifically, propagation of a crack initially placed within an ideally brittle body subject to boundary conditions in the reference configuration, $\mathscr{B}_0$, is decomposed into the crack extension in the current material domain, $\mathscr{B}_t$, and the body deformation described in the current spatial domain, Ω_t.

A different notation than the one used in [2,3] was consciously chosen here to allow for better clarity regarding the configuration to which a particular term belongs. In the present manuscript, lower case Greek subscripts will refer to the reference configuration, while upper and lower case Latin subscripts will refer to the material and the spatial configurations, respectively, see also [73,74].

A schematic representation of the ALE decomposition is illustrated in Fig. 1, where mapping at time t of reference coordinates, χ_α, to the current material coordinates, X_I, is achieved via vector-valued function $\Xi_I(\chi_\alpha, t)$ defined as:

$$\Xi_I : \mathscr{B}_0 \rightarrow \mathscr{B}_t, \quad X_I = \Xi_I(\chi_\alpha, t). \tag{1}$$

Mapping of material coordinates, X_I, onto spatial coordinates, x_i, is achieved via the deformation mapping $\varphi_i(X_I, t)$ defined as:

$$\varphi_i : \mathscr{B}_t \rightarrow \Omega_t, \quad x_i = \varphi_i(X_I, t). \tag{2}$$

The physical displacements are denoted as:

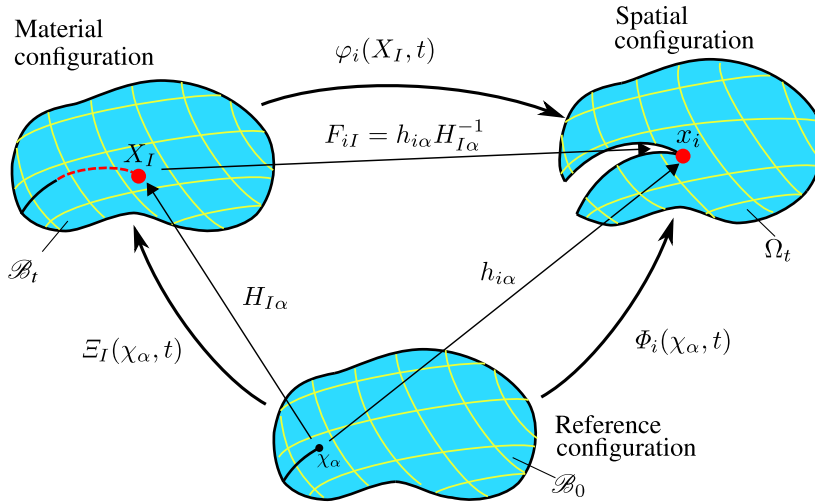$$u_i = x_i - \delta_{iI} X_I, \tag{3}$$

Fig. 1. Decomposition of crack propagation kinematics in an elastically deforming body into spatial and material displacements.

where Kronecker delta, δ_{iI}, acts as the shifter operator [73]. Note that in Eq. (3) and hereinafter the summation over the repeated indices is assumed unless otherwise stated.

Therefore, current spatial quantities can be obtained by subjecting reference quantities to Ξ_I mapping followed by φ_i mapping. Alternatively, the mapping from $\mathscr{B}_0$ to Ω_t can be directly achieved via $\Phi_i(\chi_\alpha, t)$ mapping:

$$\Phi_i : \mathscr{B}_0 \to \Omega_t, \quad x_i = \Phi_i(\chi_\alpha, t). \tag{4}$$

Two other displacement fields are defined with respect to the reference configuration:

$$W_I = X_I - \delta_{I\alpha}\chi_\alpha \quad \text{and} \quad w_i = x_i - \delta_{i\alpha}\chi_\alpha, \tag{5}$$

where W_I and w_i are the current material and current spatial displacements, respectively.

Gradients of all aforementioned mappings and the relationship that connects them can be computed as shown in [2]:

$$H_{I\alpha} = \frac{\partial X_I}{\partial \chi_\alpha}, \quad h_{i\alpha} = \frac{\partial x_i}{\partial \chi_\alpha}, \quad F_{iI} = \frac{\partial x_i}{\partial X_I} = h_{i\alpha} H_{I\alpha}^{-1}, \tag{6}$$

where the gradient of deformation, F_{iI}, is related to the gradient of material map, $H_{I\alpha}$, and the gradient of spatial map $h_{i\alpha}$ by the inverse of transformation from $\mathscr{B}_0$ to $\mathscr{B}_t$, i.e. $H_{I\alpha}^{-1}$, followed by the transformation from $\mathscr{B}_0$ to Ω_t (multiplication by $h_{i\alpha}$). Moreover, time derivatives of the displacement and the gradient of deformation at a point $X_I = \text{const}$ can be evaluated as:

$$\dot{u}_i = \dot{w}_i - F_{iJ}\dot{W}_J, \quad \dot{F}_{iJ} = \frac{\partial \dot{x}_i}{\partial X_J} = \frac{\partial \dot{u}_i}{\partial X_J} = \frac{\partial \dot{w}_i}{\partial X_J} - F_{iK}\frac{\partial \dot{W}_K}{\partial X_J}, \tag{7}$$

see [2] for more details.

2.1.2. Crack front kinematics

To analyse crack front kinematics, a crack surface $\Gamma_{\text{cr}} \in \mathscr{B}_t$ is considered to be a 2D surface embedded in 3D space. We will distinguish between two sides of Γ_{cr} representing two crack lips/sides Γ_{cr}^+ and Γ_{cr}^-, whose outward normal vectors are N_I^+ and N_I^-, respectively (see Fig. 2). Furthermore, let us consider a surface Γ_{cr}^0 that encircles the crack front denoted by $\partial\Gamma_{\text{cr}}$. Surface Γ_{cr}^0 can be seen as a cylindrical-like surface that results from a sweep of a circle of radius r with $\partial\Gamma_{\text{cr}}$ located at its centre (see Fig. 2). In the limit $r \to 0$, the surface Γ_{cr}^0 reduces to the crack front $\partial\Gamma_{\text{cr}}$, while the crack surface is obtained as $\Gamma_{\text{cr}}^+, \Gamma_{\text{cr}}^- \to \Gamma_{\text{cr}}$.

The areas of oriented crack surfaces can be calculated based on the intrinsic parametrisation (ξ_1, ξ_2), which is common to Γ_{cr}^+, Γ_{cr}^- and Γ_{cr}^0. Local tangent vectors on the oriented crack surfaces (covariant bases) are evaluated
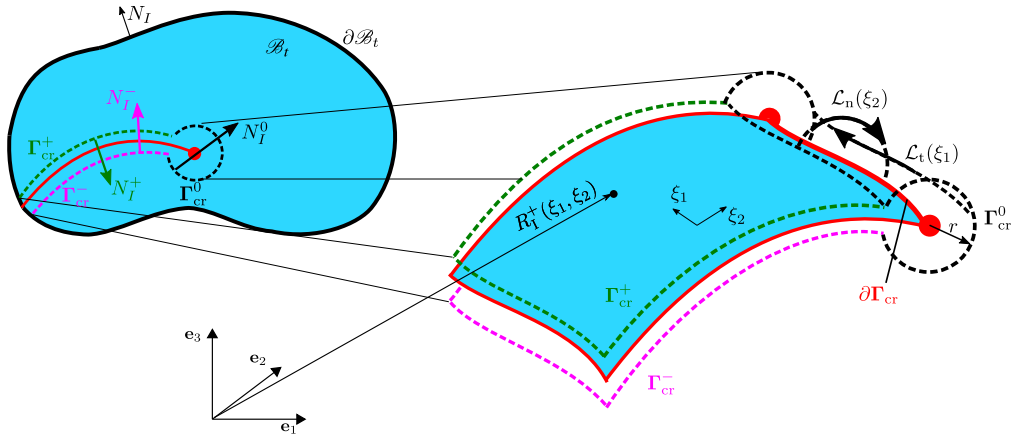
Fig. 2. Crack surface and crack front definition. *Source:* Adapted from [3]

as derivatives of the material location vector $R_I^{(m)}(\xi_1, \xi_2)$ with an arbitrary origin, where $m \in \{0, +, -\}$:

$$T_I^{(m),\xi_1} = \frac{\partial R_I^{(m)}(\xi_1, \xi_2)}{\partial \xi_1} \text{ and } T_I^{(m),\xi_2} = \frac{\partial R_I^{(m)}(\xi_1, \xi_2)}{\partial \xi_2}. \tag{8}$$

Hence, the crack surface normal vectors $N_I^{(m)}$ can be defined as:

$$N_I^{(m)} = \varepsilon_{IJK} T_J^{(m),\xi_1} T_K^{(m),\xi_2}, \tag{9}$$

where ε_{IJK} is the Levi-Civita symbol. Using (9), the crack surface area can be evaluated as:

$$A^{\Gamma_{\text{cr}}} = \lim_{r \to 0} \frac{1}{2} \sum_m^{0,+,-} A^{\Gamma_{\text{cr}}^{(m)}} = \lim_{r \to 0} \frac{1}{2} \sum_m^{0,+,-} \int_{\Gamma_{\text{cr}}^{(m)}} \left(N_I^{(m)} N_I^{(m)} \right)^{1/2} \mathrm{d}\Gamma, \tag{10}$$

while the crack surface increase rate is:

$$\begin{aligned}
\dot{A}^{\Gamma_{\text{cr}}} &= \frac{1}{2} \lim_{r \to 0} \sum_m^{0,+,-} \frac{\partial A^{\Gamma_{\text{cr}}^{(m)}}}{\partial W_J} \frac{\mathrm{d} W_J}{\mathrm{d}t} = \frac{1}{2} \lim_{r \to 0} \sum_m^{0,+,-} \int_{\Gamma_{\text{cr}}^{(m)}} \left(N_I^{(m)} N_I^{(m)} \right)^{-1/2} N_I^{(m)} \frac{\partial N_I^{(m)}}{\partial W_J} \dot{W}_J \, \mathrm{d}\Gamma \\
&= \frac{1}{2} \lim_{r \to 0} \sum_m^{0,+,-} \int_{\Gamma_{\text{cr}}^{(m)}} A_J^{\Gamma_{\text{cr}}^{(m)}} \dot{W}_J \, \mathrm{d}\Gamma.
\end{aligned} \tag{11}$$

The vector $A_J^{\Gamma_{\text{cr}}^{(m)}}$ is defined as:

$$A_J^{\Gamma_{\text{cr}}^{(m)}} := \hat{N}_I^{(m)} \frac{\partial N_I^{(m)}}{\partial W_J}, \tag{12}$$

where $\hat{N}_I^{(m)}$ is the unit normal vector:

$$\hat{N}_I^{(m)} = \frac{N_I^{(m)}}{\| N_I^{(m)} \|}. \tag{13}$$

It is important to note that any increase of the crack surface area can occur only at the crack front, i.e. the material velocity $\dot{W}_J$ is non-zero only on $\partial \Gamma_{\text{cr}}$. Therefore, the expression (11) can be rewritten as:

$$\dot{A}^{\Gamma_{\text{cr}}} = \frac{1}{2} \lim_{r \to 0} \int_{\Gamma_{\text{cr}}^0} A_J^{\Gamma_{\text{cr}}^0} \dot{W}_J \, \mathrm{d}\Gamma = \int_{\mathcal{L}_t} \frac{1}{2} \lim_{r \to 0} \oint_{\mathcal{L}_n} A_J^{\Gamma_{\text{cr}}^0} \dot{W}_J \, \mathrm{d}\mathcal{L}_n \mathrm{d}\mathcal{L}_t = \int_{\mathcal{L}_t} A_J^{\partial \Gamma_{\text{cr}}} \dot{W}_J \, \mathrm{d}\mathcal{L}_t, \tag{14}$$

where we used parametrisation $\mathcal{L}_t(\xi_1) = \Gamma_{\text{cr}}^0(\xi_1, \xi_2)|_{\xi_2 = \text{const}}$ and $\mathcal{L}_n(\xi_2) = \Gamma_{\text{cr}}^0(\xi_1, \xi_2)|_{\xi_1 = \text{const}}$ (see Fig. 2). Since the material velocity $\dot{W}_J$ does not change with respect to ξ_2 parameter when $|\mathcal{L}_n| \to 0$, we introduced in (14) a unitless

kinematic state variable $A_J^{\partial \Gamma_{\mathrm{cr}}}$ that defines the direction of the crack front extension:

$$A_J^{\partial \Gamma_{\mathrm{cr}}} := \frac{1}{2} \lim_{r \to 0} \oint_{\mathcal{L}_{\mathrm{n}}} A_J^{\Gamma_{\mathrm{cr}}^0} \mathrm{d}\mathcal{L}_{\mathrm{n}}. \tag{15}$$

2.2. Power balance in a cracked body

The crack propagation problem can be considered as a thermodynamic system including a solid deformable body with an imperfection. Traction applied on the boundary of the body $\partial \mathcal{B}_t$ performs the work on the system. We may express the power input into the body in terms of spatial velocity $\dot{u}_i$ and traction $t_i = \delta_{iJ} T_J$ as:

$$\mathscr{P} := \int_{\Gamma_\sigma} \dot{u}_i t_i \mathrm{d}\Gamma = \int_{\Gamma_\sigma} \left(\dot{w}_i t_i - \dot{W}_K F_{Ki} t_i \right) \mathrm{d}\Gamma, \tag{16}$$

where (7) was used, and T_J is a traction defined on the surface $\Gamma_\sigma \subset \partial \mathcal{B}_t$ in the material configuration.

Following the first law of thermodynamics, the power of external work on elastic body must be balanced by the sum of the crack energy release rate, $\dot{\mathscr{U}}_{\Gamma_{\mathrm{cr}}}$, and the rate of change of the internal body energy, $\dot{\mathscr{U}}_{\mathcal{B}_t}$:

$$\mathscr{P} = \dot{\mathscr{U}}_{\Gamma_{\mathrm{cr}}} + \dot{\mathscr{U}}_{\mathcal{B}_t}, \tag{17}$$

where the terms on the right-hand side are defined as:

$$\mathscr{U}_{\Gamma_{\mathrm{cr}}} := \gamma_{\mathrm{cr}} A^{\Gamma_{\mathrm{cr}}} \quad \text{and} \quad \mathscr{U}_{\mathcal{B}_t} := \int_{\mathcal{B}_t} \Psi(F_{iJ}) \mathrm{d}V, \tag{18}$$

with γ_{cr} and Ψ being the surface energy and the free energy density function, respectively. Substituting expressions (16) and (18) into (17) and taking into account time derivatives presented in (7) and (14), given that $\mathrm{d}\dot{V} = \partial \dot{W}_I / \partial X_I \mathrm{d}V$, yields:

$$\int_{\Gamma_\sigma} \left(\dot{w}_i t_i - \dot{W}_J F_{Ji} t_i \right) \mathrm{d}\Gamma = \gamma_{\mathrm{cr}} \int_{\partial \Gamma_{\mathrm{cr}}} A_I^{\partial \Gamma_{\mathrm{cr}}} \dot{W}_I \mathrm{d}\partial\Gamma + \int_{\mathcal{B}_t} \left(P_{iJ} \frac{\partial \dot{w}_i}{\partial X_J} + \Sigma_{KJ} \frac{\partial \dot{W}_K}{\partial X_J} \right) \mathrm{d}V, \tag{19}$$

where

$$P_{iJ} := \frac{\partial \Psi(F_{iJ})}{\partial F_{iJ}} \quad \text{and} \quad \Sigma_{KJ} := \Psi(F_{iJ}) \delta_{KJ} - F_{Kk} P_{kJ} \tag{20}$$

are first Piola–Kirchhoff stress tensor and Eshelby stress tensor [26,75], respectively. By applying the divergence theorem, Eq. (19) can be rewritten as:

$$\gamma_{\mathrm{cr}} \int_{\partial \Gamma_{\mathrm{cr}}} A_I^{\partial \Gamma_{\mathrm{cr}}} \dot{W}_I \mathrm{d}\partial\Gamma = \int_{\mathcal{B}_t} \left(\dot{w}_i \frac{\partial P_{iJ}}{\partial X_J} + \dot{W}_K \frac{\partial \Sigma_{KJ}}{\partial X_J} \right) \mathrm{d}V$$
$$+ \int_{\Gamma_\sigma} \dot{w}_i \left(t_i - P_{iJ} \hat{N}_J \right) \mathrm{d}\Gamma - \int_{\Gamma_\sigma} \dot{W}_K \left(F_{Ki} t_i + \Sigma_{KJ} \hat{N}_J \right) \mathrm{d}\Gamma \tag{21}$$
$$- \int_{\partial \Gamma_{\mathrm{cr}}} \dot{w}_i \left(\lim_{r \to 0} \oint_{\mathcal{L}_{\mathrm{n}}} P_{iJ} \hat{N}_J \, \mathrm{d}\mathcal{L}_{\mathrm{n}} \right) \mathrm{d}\partial\Gamma - \int_{\partial \Gamma_{\mathrm{cr}}} \dot{W}_K \left(\lim_{r \to 0} \oint_{\mathcal{L}_{\mathrm{n}}} \Sigma_{KJ} \hat{N}_J \, \mathrm{d}\mathcal{L}_{\mathrm{n}} \right) \mathrm{d}\partial\Gamma.$$

The conservation of linear momentum, complimented by the equilibrium of stress with external forces on the surface of the body, reads:

$$\frac{\partial P_{iJ}}{\partial X_J} = 0 \text{ in } \mathcal{B}_t, \quad P_{iJ} \hat{N}_J = t_i \text{ on } \Gamma_\sigma. \tag{22}$$

Note that inertia terms are neglected and we restrict ourselves to quasi-static problems. Moreover, linear material momentum balance is similarly expressed as:

$$\frac{\partial \Sigma_{KJ}}{\partial X_J} = 0 \text{ in } \mathcal{B}_t, \quad \Sigma_{KJ} \hat{N}_J = -F_{Ki} t_i \text{ on } \Gamma_\sigma, \tag{23}$$

according to the derivation presented in [26,76]. Making use of (22)–(23) and noting that the surface $\mathcal{L}_{\mathrm{n}}$ surrounding the crack front is traction-free, (21) reduces to:

$$\gamma_{\mathrm{cr}} \int_{\partial \Gamma_{\mathrm{cr}}} A_K^{\partial \Gamma_{\mathrm{cr}}} \dot{W}_K \mathrm{d}\partial\Gamma + \int_{\partial \Gamma_{\mathrm{cr}}} \dot{W}_K \left(\lim_{r \to 0} \oint_{\mathcal{L}_{\mathrm{n}}} \Sigma_{KJ} \hat{N}_J \, \mathrm{d}\mathcal{L}_{\mathrm{n}} \right) \mathrm{d}\partial\Gamma = 0. \tag{24}$$

Therefore, the equilibrium equation for the crack front takes the form:

$$\dot{W}_K \left(\gamma_{\mathrm{cr}} A_K^{\partial \Gamma_{\mathrm{cr}}} - G_K^{\partial \Gamma_{\mathrm{cr}}} \right) = 0, \tag{25}$$

where

$$G_K^{\partial \Gamma_{\mathrm{cr}}} := -\lim_{r \to 0} \oint_{\mathcal{L}_{\mathrm{n}}} \Sigma_{KJ} \hat{N}_J \mathrm{d}L_{\mathrm{n}} \tag{26}$$

is the configurational (material) force resulting from external loads.

Three possible cases emerge from (25) for the crack front to be in equilibrium. The first case involves the crack front material velocities, $\dot{W}_K$, to be zero and therefore the crack is not propagating. The second case results in crack propagation when $\dot{W}_K \neq 0$ and the scaled crack extension vector, $\gamma_{\mathrm{cr}} A_K^{\partial \Gamma_{\mathrm{cr}}}$ is equal to the configurational force $G_K^{\partial \Gamma_{\mathrm{cr}}}$. The third case is when the $\dot{W}_K$ is perpendicular to $\gamma_{\mathrm{cr}} A_K^{\partial \Gamma_{\mathrm{cr}}} - G_K^{\partial \Gamma_{\mathrm{cr}}}$, i.e. crack does not propagate. The following subsection is devoted to the discussion of the crack propagation constraints permitting to select the appropriate case from these three possibilities.

2.3. Crack propagation constraints

To be able to select between the cases resulting from (25), we will use an appropriate criterion for linearly elastic fully brittle material. Following [2,3], we consider a generalisation of the classic Griffith's criterion for the case of a non-straight crack front in a 3D body:

$$f(G_K^{\partial \Gamma_{\mathrm{cr}}}) := A_K^{\partial \Gamma_{\mathrm{cr}}} \left(G_K^{\partial \Gamma_{\mathrm{cr}}} - A_K^{\partial \Gamma_{\mathrm{cr}}} g_{\mathrm{cr}}/2 \right) \leq 0, \tag{27}$$

where the material parameter $g_{\mathrm{cr}} = 2\gamma_{\mathrm{cr}}$ is the so-called Griffith energy that represents the threshold surface energy which the crack front $\partial \Gamma_{\mathrm{cr}}$ can withstand before the crack can propagate.

The dissipation of energy per unit length of the crack front can be evaluated as $\mathcal{D} := G_K^{\partial \Gamma_{\mathrm{cr}}} \dot{W}_K$. For the solution branch where the crack is propagating, we need to enforce an admissible thermodynamic process with positive energy dissipation, i.e. $\mathcal{D} \geq 0$. Furthermore, from all admissible processes we will choose the one which dissipates energy maximally and at the same time fulfils the Griffith criterion (27). Such process can be expressed as the solution of the following saddle point problem:

$$\min_{G_K^{\partial \Gamma_{\mathrm{cr}}}} \max_{\dot{\kappa}} \mathcal{L}, \quad \mathcal{L} := -G_K^{\partial \Gamma_{\mathrm{cr}}} \dot{W}_K + \dot{\kappa} f(G_K^{\partial \Gamma_{\mathrm{cr}}}), \tag{28}$$

where a Lagrange multiplier field $\dot{\kappa} \geq 0$ is a kinematic variable, dual to a static variable $G_K^{\partial \Gamma_{\mathrm{cr}}}$. The saddle point problem (28) is associated with the following Karush–Kuhn–Tucker (KKT) conditions:

$$\dot{\kappa} \geq 0, \quad f(G_K^{\partial \Gamma_{\mathrm{cr}}}) \leq 0, \quad \dot{\kappa} f(G_K^{\partial \Gamma_{\mathrm{cr}}}) = 0. \tag{29}$$

It is important to note that the numerical implementation of KKT conditions (29) is inconvenient: one would need to compute $G_K^{\partial \Gamma_{\mathrm{cr}}}$ at the crack front. This could be calculated numerically using the path-independent J-integral [7,8,77], or by integration of Eshelby stress in the volume [28,29]. However, both approaches lead to implementation challenges, especially for an implicit crack propagation scheme.

Instead, we transform the KKT conditions (29) to remove the dependence on $G_K^{\partial \Gamma_{\mathrm{cr}}}$ while preserving a single Lagrange multiplier field to maintain the well-posedness of the saddle point problem (28). This transformation is based on two observations. The first follows from the Griffith's criterion (27) and involves the force balance at the crack front which can be expressed as (see also Fig. 3):

$$G_K^{\partial \Gamma_{\mathrm{cr}}} - (g_{\mathrm{cr}}/2 - \rho) A_K^{\partial \Gamma_{\mathrm{cr}}} = 0, \tag{30}$$

where ρ is a new variable which scales $A_K^{\partial \Gamma_{\mathrm{cr}}}$ such that (30) is fulfilled. Three cases following from (30) can be distinguished: (i) $\rho = g_{\mathrm{cr}}/2$ when the body is not loaded, i.e. $G_K^{\partial \Gamma_{\mathrm{cr}}} = 0$; (ii) $\rho = 0$ when the crack propagates; and an intermediate state (iii) when $G_K^{\partial \Gamma_{\mathrm{cr}}} \neq 0$ and $\rho > 0$. Moreover, (30) implies that $G_K^{\partial \Gamma_{\mathrm{cr}}}$ is co-linear to $A_K^{\partial \Gamma_{\mathrm{cr}}}$: when the crack propagates in case (ii), collinearity is already dictated by the equilibrium equation for the crack front (25), while the collinearity of $G_K^{\partial \Gamma_{\mathrm{cr}}}$ and $A_K^{\partial \Gamma_{\mathrm{cr}}}$ for the case (iii), when the crack does not propagate, is an assumption we introduce.
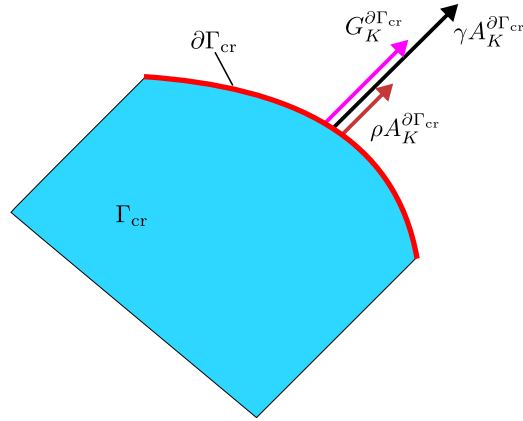
Fig. 3. Schematic of the forces in balance at the crack front.

The second observation follows from finding the stationary point of the Lagrangian in (28) with respect to $G_K^{\partial\Gamma_{\mathrm{cr}}}$, which leads to the following identity:

$$\dot{W}_K = \dot{\kappa} A_K^{\partial\Gamma_{\mathrm{cr}}}. \tag{31}$$

Note that $A_K^{\partial\Gamma_{\mathrm{cr}}} A_K^{\partial\Gamma_{\mathrm{cr}}} \geq 0$, and hence for $\dot{\kappa} \geq 0$, $\dot{\kappa} A_K^{\partial\Gamma_{\mathrm{cr}}} A_K^{\partial\Gamma_{\mathrm{cr}}} = A_K^{\partial\Gamma_{\mathrm{cr}}} \dot{W}_K \geq 0$. Following these two observations, the KKT conditions (29) can be transformed into the new form:

$$A_K^{\partial\Gamma_{\mathrm{cr}}} \dot{W}_K \geq 0, \qquad \rho \geq 0, \qquad \rho A_K^{\partial\Gamma_{\mathrm{cr}}} \dot{W}_K = 0. \tag{32}$$

The KKT conditions (32) can be enforced by the active set method with a complementarity function similar to the one proposed for frictionless contact constraints [37]:

$$C_{\mathrm{cr}}(\rho, \dot{W}_K) := \rho - \max\left(0, \rho - c_{\mathrm{cr}} A_K^{\partial\Gamma_{\mathrm{cr}}} \dot{W}_K\right), \tag{33}$$

where c_{cr} is the stability/complementarity parameter, controlling convergence of the Newton–Raphson method and is chosen in range of the Griffith energy of a given material. In the developed framework, equation $C_{\mathrm{cr}}(\rho, \dot{W}_K) = 0$ is solved together with the crack front balance equation (30).

2.4. Additional boundary conditions in the material domain

To impose shape preservation of the cracked body in the material configuration [3], we consider additional essential boundary conditions which complement (23) on the whole boundary except the crack front:

$$[X_I - \chi_\alpha \delta_{\alpha I}] \hat{N}_I = 0 \quad \text{on } (\partial\mathscr{B}_t \cup \Gamma_{\mathrm{cr}}^+ \cup \Gamma_{\mathrm{cr}}^-) \setminus \partial\Gamma_{\mathrm{cr}}, \tag{34}$$

see also Fig. 4(a). Furthermore, since sliding of material points along the boundary surfaces does not generate configurational changes in a homogeneous material, additional natural boundary conditions are applied as follows:

$$\Sigma_{KJ} \hat{N}_J (\delta_{KL} - \hat{N}_K \hat{N}_L) = \{0, 0, 0\} \quad \text{on } (\partial\mathscr{B}_t \cup \Gamma_{\mathrm{cr}}^+ \cup \Gamma_{\mathrm{cr}}^-) \setminus (\partial\Gamma_{\mathrm{cr}} \cup \Gamma_\sigma), \tag{35}$$

i.e. on the whole boundary except the trace of the crack front and the regions where the natural boundary conditions are imposed.

2.5. Contact constraints

Unilateral contact of two 3D elastic bodies is schematically presented in Fig. 4(b). Two contacting bodies are termed as slave and master, and associated quantities are denoted by superscripts (1) and (2), respectively, e.g. the two bodies are denoted by $\Omega^{(i)}$, where $i = 1$ or 2. Furthermore, each body's surface, $\partial\Omega^{(i)}$, is divided into three sets
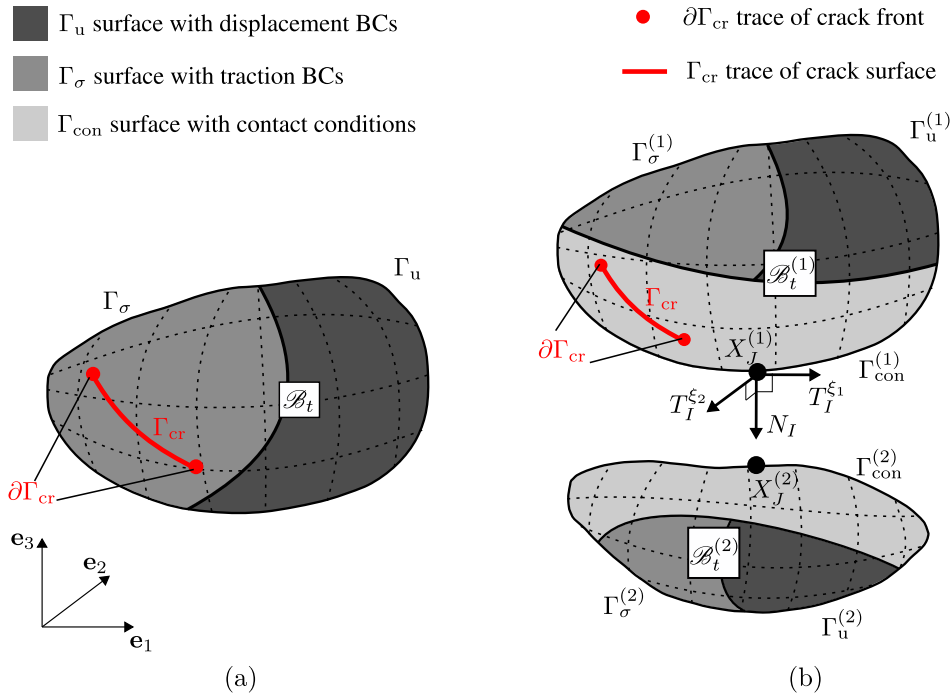
Fig. 4. Schematic representation of 3D bodies: (a) a cracked body with traction and displacements boundary conditions and (b) a cracked and an intact body coming into contact (presented as separated to provide a clearer visual impression).

depending on the boundary conditions applied to its regions, i.e. essential boundary $\Gamma_u^{(i)}$, natural boundary $\Gamma_\sigma^{(i)}$ and contact boundary $\Gamma_c^{(i)}$. Following assumptions presented in [39,78], these boundary sets are considered as disjoint.

In the schematic example in Fig. 4(b), point $X_J^{(1)}$, located on the slave surface, and point $X_J^{(2)}$, located on the master surface, are in contact. Since applications considered in this work can be studied under small displacements and small strains assumptions, current and material configurations are considered to be indistinguishable. Therefore, the outer normal vector, N_I, and tangent vectors, $T_I^{\xi_1}$ and $T_I^{\xi_2}$, are chosen to be functions of the material coordinates $X_J^{(1)}$. The normal is then defined as:

$$N_I(X_J^{(1)}) = \varepsilon_{IKL} T_K^{\xi_1} T_L^{\xi_2}, \tag{36}$$

and the unit normal $\hat{N}_I(X_J^{(1)})$ is evaluated according to Eq. (13). However, it is important to note that all previously discussed theoretical formulations are valid for large strains and large displacements. In order to make the contact formulation presented below valid for these cases, one would only need to consider normal and tangent vectors as functions of the spatial coordinates x_j.

The gap between the two bodies is evaluated based on the current position of two points $x_j^{(1)}$ and $x_j^{(2)}$ and is defined using a scalar gap function:

$$g_{\text{con}}(x_j^{(i)}, X_J^{(1)}) = -\hat{N}_I\left(X_J^{(1)}\right) \delta_{Ij}\left[x_j^{(1)} - x_j^{(2)}\right], \tag{37}$$

and as the gap function and normal vector will always be defined on the slave surface, the superscript (1) is dropped for these terms.

Since the present paper focuses on frictionless contact, only normal component, p_{con}, of current contact traction, t_j^c, over the slave surface area is taken into account and evaluated as

$$p_{\text{con}} = t_j^c \delta_{jJ} \hat{N}_J. \tag{38}$$

Then, the conditions that describe frictionless contact in the absence of adhesion can be expressed in the form of the Karush–Kuhn–Tucker (KKT) conditions as

$$g_{\text{con}} \geq 0, \qquad p_{\text{con}} \leq 0, \qquad p_{\text{con}}g_{\text{con}} = 0, \tag{39}$$

where the tension-positive convention is considered. We follow [37] and enforce KKT conditions by considering the complementarity function:

$$C_{\text{con}}(\lambda, x_j^{(i)}, X_J^{(1)}) := \lambda - \max\left(0, \lambda - c_{\text{n}}g_{\text{con}}\right), \tag{40}$$

where c_{n} is a stabilisation/complementarity parameter that has a similar sense to the augmentation parameter in the augmented Lagrangian method [36,79]. Moreover, λ is a scalar Lagrange multiplier function which is introduced to fulfil the KKT conditions and is defined with respect to contact normal traction as $\lambda = -p_{\text{con}}$. The KKT conditions are then fulfilled when $C_{\text{con}}(\lambda, x_j^{(i)}, X_J^{(1)}) = 0$.

3. Variational expression for governing equations

This section presents the variational form of the governing equations for crack propagation, traction and contact conditions, presented in Section 2. Note that a quasi-static formulation was chosen to be developed. The discretisation versions of the terms shown here are discussed in subsequent Section 4.

3.1. Variational formulation for crack propagation problem

First, we will consider the weak form of the crack front balance equation (30). The virtual work of the material force can be computed as the integral of $G_K^{\partial\Gamma_{\text{cr}}}$ along the crack front, see Eq. (26), weighted by the variation of material displacements:

$$\delta\mathscr{F} := -\int_{\partial\Gamma_{\text{cr}}} \delta X_K \left(\lim_{r \to 0} \oint_{\mathcal{L}_{\text{n}}} \Sigma_{KJ}\hat{N}_J \mathrm{d}L_{\text{n}}\right) \mathrm{d}\partial\Gamma = -\int_{\mathcal{B}_t} \frac{\partial \delta X_K}{\partial \chi_\beta} \delta_{\beta J}\Sigma_{KJ}\mathrm{d}\Omega, \tag{41}$$

where the divergence theorem was applied and then (23) was used.

The virtual work of the material resistance force at the crack front is computed similarly as:

$$\delta\mathscr{M} := \int_{\partial\Gamma_{\text{cr}}} \delta X_K A_K^{\partial\Gamma_{\text{cr}}}(\rho - g_{\text{cr}}/2)\mathrm{d}\partial\Gamma, \tag{42}$$

where $A_K^{\partial\Gamma_{\text{cr}}}$ was defined in (15). Finally, to obtain the variational form of the crack front propagation conditions (32), we integrate the complementarity function (33) multiplied by the variation of the variable ρ:

$$\delta\mathscr{C}_{\text{cr}} := \int_{\partial\Gamma_{\text{cr}}} \delta\rho\, C_{\text{cr}}(\rho, \Delta W_I^t)\mathrm{d}\partial\Gamma, \tag{43}$$

where $\Delta W_I^t = X_I^t - X_I^{t-1}$ is the crack front displacement increment at load step t.

3.2. Variational form of surface traction terms

Traction BCs are presented in Eqs. (22) (spatial forces) and (23) (material forces). The virtual work input of traction can be expressed with two terms associated with variations of spatial and material positions as:

$$\delta\mathscr{T}^{\text{sp}} := \int_{\Gamma_\sigma} \delta x_i t_i \mathrm{d}\Gamma, \qquad \delta\mathscr{T}^{\text{mat}} := -\int_{\Gamma_\sigma} \delta X_K F_{Ki} t_i \mathrm{d}\Gamma, \tag{44}$$

where $\delta\mathscr{T}^{\text{sp}}$ and $\delta\mathscr{T}^{\text{mat}}$ represent the virtual work of traction in spatial and material configurations, respectively.

3.3. Variational formulation of contact constraints

First, the virtual work terms of the contact pressure associated with variation of spatial positions on the master and slave bodies are expressed as:

$$\delta\mathscr{Q}^{(1)} := \int_{\partial\Gamma_{\text{con}}^{(1)}} \delta x_i^{(1)}\delta_{iI}\lambda\hat{N}_I \mathrm{d}\Gamma, \qquad \delta\mathscr{Q}^{(2)} := -\int_{\partial\Gamma_{\text{con}}^{(2)}} \delta x_i^{(2)}\delta_{iI}\lambda\hat{N}_I \mathrm{d}\Gamma. \tag{45}$$

Furthermore, the complementarity function presented in (40) is weighted by the test functions, $\delta\lambda$, of contact Lagrange multipliers, and the corresponding variational form is defined as:

$$\delta\mathscr{C}_{\mathrm{con}} := \int_{\partial\Gamma_{\mathrm{con}}^{(1)}} \delta\lambda C_{\mathrm{con}} \mathrm{d}\Gamma. \tag{46}$$

Similarly to the additional term associated with virtual material displacements in (44), the virtual work of contact pressure in the material configuration is defined as:

$$\delta\mathscr{R}^{(i)} := (-1)^i \int_{\Gamma_{\mathrm{con}}^{(i)}} \delta X_I^{(i)} F_{Ii} \delta_{iJ} \lambda \hat{N}_J \mathrm{d}\partial\Gamma, \tag{47}$$

where $i = 1$ or 2 when the crack front is propagating along the slave or master contact surface, respectively.

4. Problem discretisation and implementation

In this section we will discretise the problem using finite elements by means of the Galerkin method for the case of tetrahedral FE meshes. The assembly of the emerging system of equations is denoted here by various assembly operators A. While degrees of freedom (DOFs) of multiple unknown fields considered here correspond to certain algebraic entries of the resulting system of equations, these DOFs are also associated with certain mesh entities. Therefore, to clarify the description, for each assembly operator we will specify the associated geometric entities. For instance, operator $\mathrm{A}_{\partial\mathscr{B}_t^h \cap \partial\Gamma_{\mathrm{cr}}^h}$ denotes the assembly of algebraic entries corresponding to DOFs associated with the geometric entities on the intersection between the discretised boundary of the body and the crack front. This is eventually the trace of the crack front on the body surface. Note that the superscript h is used hereinafter to denote discretised versions of geometrical entities.

Note also that the theoretical formulations presented in Sections 2 and 3 are general, however, the finite element implementation described below is done under the assumption of small strains and small displacements.

4.1. Crack propagation problem discretisation and resolution of propagating crack

The spatial and material position fields are approximated according to the finite element method as:

$$x_i^h = \sum_{s=1}^{n_{\mathrm{sp}}} S^s \tilde{x}_i^s, \quad X_I^h = \sum_{m=1}^{n_{\mathrm{mat}}} M^m \tilde{X}_I^m, \tag{48}$$

where superscript h refers to the field approximation and $(\tilde{\cdot})$ denotes degrees of freedom. Moreover, S^s, $M^m \in H^1(\Omega^h)$ are spatial and material polynomial scalar base functions, respectively, which are conforming within the FE mesh. For spatial positions, hierarchical basis functions proposed in [80] for tetrahedral elements are chosen in the present work to allow for spatially heterogeneous approximation order. This feature is particularly useful for solving the crack propagation problem since approximation order can be seamlessly increased near the crack front to improve approximation quality. At the same time, in the present work, first order of approximation is chosen for material positions which is sufficient to approximate the geometry of the crack front. Therefore, the total number of spatial base functions is greater or equal to the material base functions, i.e. $n_{\mathrm{sp}} \geq n_{\mathrm{mat}}$ in Eq. (48). Accordingly, the discretised versions of the three gradients of deformation presented in (6) are:

$$H_{I\alpha}^h = \sum_{m=1}^{n_{\mathrm{mat}}} \frac{\partial M^m}{\partial \chi_\alpha} \tilde{X}_I^m, \quad h_{i\alpha}^h = \sum_{s=1}^{n_{\mathrm{sp}}} \frac{\partial S^s}{\partial \chi_\alpha} \tilde{x}_i^s, \quad F_{iI}^h = \left(\sum_{s=1}^{n_{\mathrm{sp}}} \frac{\partial S^s}{\partial \chi_\alpha} \tilde{x}_i^s\right)\left(\sum_{m=1}^{n_{\mathrm{mat}}} \frac{\partial M^m}{\partial \chi_\alpha} \tilde{X}_I^m\right)^{-1}. \tag{49}$$

4.1.1. Crack propagation problem discretisation

Contribution to the residual vector from the virtual work term (41) of the crack front balance equation can be expressed as:

$$\mathscr{F}_I^m := -\mathop{\mathrm{A}}_{\partial\Gamma_{\mathrm{cr}}^h} \int_{\mathscr{B}_{t,\mathrm{cf}}^h} \frac{\partial M^m}{\partial X_K} \Sigma_{IK}^h \mathrm{d}\Omega^h, \tag{50}$$
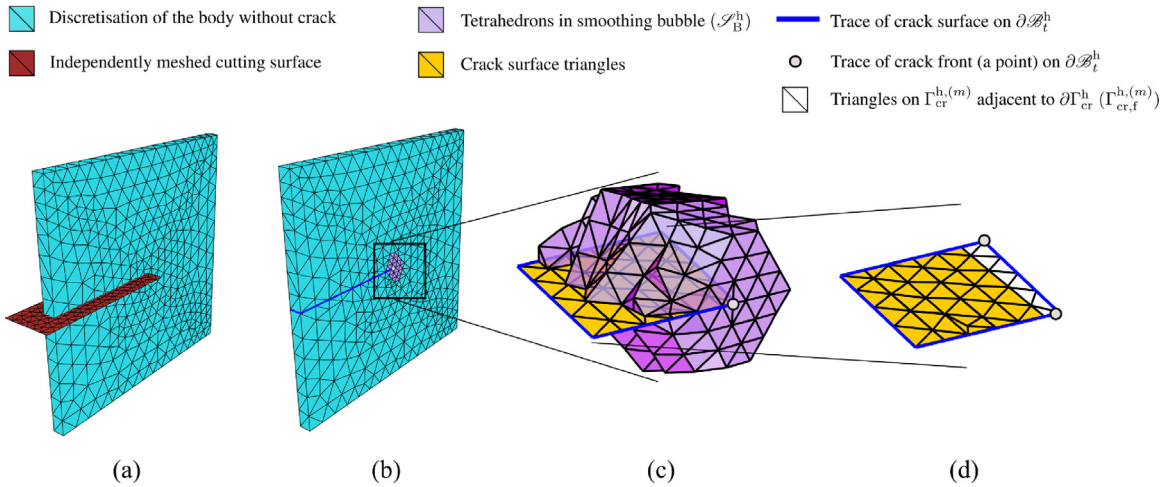
Fig. 5. Schematic of: (a) initial mesh used for crack propagation analysis where the discretised body is generated independently from the cutting surface used to seed the crack, (b) mesh seeded with initial crack based on the cutting surface, (c) a zoom at the vicinity of the crack front after mesh cutting has been performed where only the resulting crack surface and smoothing bubble (see definition in Section 4.1.2) are presented and (d) only the crack surface with highlighted triangles adjacent to crack front.

where the integration domain $\mathscr{B}^{\mathrm{h}}_{t,\mathrm{cf}}$ represents a single layer of tetrahedral elements adjacent to the crack front, while the assembly is done to algebraic entries of the system associated with the nodes of the crack front. Note that the integration domain presented in (41) is reduced to $\mathscr{B}^{\mathrm{h}}_{t,\mathrm{cf}}$ since it is the support for test functions δX^{h}_I.

The contribution of the term (42) of the crack front balance equation reads:

$$\mathscr{M}^m_I := \underset{\partial \Gamma^{\mathrm{h}}_{\mathrm{cr}}}{\mathbf{A}} \int_{\partial \Gamma^{\mathrm{h}}_{\mathrm{cr}}} M^m A^{\mathrm{h},\partial \Gamma_{\mathrm{cr}}}_I (\rho^{\mathrm{h}} - g^{\mathrm{h}}_{\mathrm{cr}}/2) \mathrm{d}\partial \Gamma^{\mathrm{h}} = \underset{\partial \Gamma^{\mathrm{h}}_{\mathrm{cr}}}{\mathbf{A}} \int_{-1}^{1} M^m M^c \tilde{A}^{\partial \Gamma_{\mathrm{cr}},c}_I (\rho^{\mathrm{h}} - g^{\mathrm{h}}_{\mathrm{cr}}/2) \mathrm{d}\eta, \tag{51}$$

where $\rho^{\mathrm{h}} := \sum_{c=1}^{n_{\mathrm{fr}}} M^c \tilde{\rho}^c$, $\tilde{\rho}^c$ is the value of the DOF for the crack front Lagrange multiplier, n_{fr} is the total number of crack front nodes and $g^{\mathrm{h}}_{\mathrm{cr}}$ is the approximated Griffith energy value which depends on the material coordinates for heterogeneous materials [72]. Since only homogeneous materials are considered in this work, no further consideration of $g^{\mathrm{h}}_{\mathrm{cr}}$ is needed as it is constant throughout the material domain.

Moreover, in the discrete setting of finite elements approximation, crack surface is represented by face elements, e.g. triangles. As a consequence, we cannot directly represent $A^{\partial \Gamma_{\mathrm{cr}}}_I$ in (15) since the limit for discrete representation of the crack surface cannot be calculated. Instead, we introduce a nodal quantity $\tilde{A}^{\partial \Gamma_{\mathrm{cr}},c}_I$, as proposed in [2], which provides the connection between the variation of the crack surface area $\delta A^{\Gamma_{\mathrm{cr}}}$ and the variation of the material displacement of nodes:

$$\delta A^{\Gamma_{\mathrm{cr}}} = \sum_{c=1}^{n_{\mathrm{cr}}} \tilde{A}^{\partial \Gamma_{\mathrm{cr}},c}_I \delta \tilde{X}^c_I, \quad \tilde{A}^{\partial \Gamma_{\mathrm{cr}},c}_I := \frac{1}{2} \sum_{n}^{+,-} \int_{\Gamma^{\mathrm{h},(n)}_{\mathrm{cr,f}}} \hat{N}^{\mathrm{h},(n)}_J \frac{\partial N^{\mathrm{h},(n)}_J}{\partial \tilde{X}^c_I} \mathrm{d}\Gamma, \tag{52}$$

where the integration is performed on both sides of the crack surface over the triangles adjacent to the crack front $\partial \Gamma^{\mathrm{h}}_{\mathrm{cr}}$, which are denoted as $\Gamma^{\mathrm{h},(n)}_{\mathrm{cr,f}}$, see Fig. 5(d). The determinant of the Jacobian (i.e. the length of the crack front edge) is not present under the parent space integral in (51) since this length is already accounted in the term $\tilde{A}^{\partial \Gamma_{\mathrm{cr}},c}_I$ defined in (52). Furthermore, the direction of the crack front extension in the continuum representation in (15) can change non-smoothly, however, in the discrete setting (52), crack front can extend only in a smooth manner. The normal vector $N^{\mathrm{h}}_J(X^{\mathrm{h}}_J)$ and the unit normal vector $\hat{N}^{\mathrm{h}}_J(X^{\mathrm{h}}_J)$ to the triangular surface on $\partial \mathscr{B}^{\mathrm{h}}_t$ are calculated as:

$$N^{\mathrm{h}}_I(X^{\mathrm{h}}_J) = \varepsilon_{IKL} T^{\mathrm{h},\xi_1}_K T^{\mathrm{h},\xi_2}_L = \varepsilon_{IKL} \left(\sum_{m=1}^{n_{\mathrm{mat}}} \frac{\partial M^m}{\partial \xi_1} \tilde{X}^m_K \right) \left(\sum_{m=1}^{n_{\mathrm{mat}}} \frac{\partial M^m}{\partial \xi_2} \tilde{X}^m_L \right) \text{ and } \hat{N}^{\mathrm{h}}_I(X^{\mathrm{h}}_J) = \frac{N^{\mathrm{h}}_I(X^{\mathrm{h}}_J)}{\|N^{\mathrm{h}}_J(X^{\mathrm{h}}_J)\|}, \tag{53}$$

respectively.

Finally, the contribution to the residual vector from the virtual work associated with elastic stress in the whole volume of the body reads:

$$f_i^{\mathrm{sp},s} := \mathop{\mathbf{A}}_{\mathscr{B}_t^{\mathrm{h}}} \int_{\mathscr{B}_t^{\mathrm{h}}} \frac{\partial S^s}{\partial X_J} P_{iJ}^{\mathrm{h}} \mathrm{d}\Omega^{\mathrm{h}}, \tag{54}$$

which results from the standard finite element procedure applied to the balance of linear momentum equation in (22).

4.1.2. Resolution of propagating crack

In the present work, a new procedure is proposed for resolving mesh evolution caused by propagating crack. It is important to note, that the implementation of the presented approach has immediate implications on resolving crack propagation which is linked to the handling of traction and contact boundary conditions in the ALE formalism; the details will be described in Section 4.2.

At the start of the crack propagation analysis a mesh of an ideally brittle body and a separately discretised cutting surface are provided, see Fig. 5(a). Thereafter, the cutting surface is used to cut the mesh of the brittle body following the strategy described in [3]. Once the intact mesh is cut, the crack propagation analysis proceeds by keeping the same mesh topology for n_{steps} number of steps chosen by the user. After these steps, the mesh cutting is repeated again, now using an updated crack surface for the cutting, which is followed by another n_{steps} steps of crack propagation. This cyclic procedure is repeated while the crack propagation is topologically possible.

It is important to highlight the distinction between evolution of the current material configuration and that of the mesh topology. When the crack propagates, it passes through current material points X_I^{h} resulting in a discontinuity in the mapping between current material configuration $\Xi_I(\chi_\alpha^{\mathrm{h}}, t)$ and spatial configuration $\varphi_i(X_I^{\mathrm{h}}, t)$. This is an evolution of the material configuration. However, during the n_{steps} of propagation, mesh topology is not evolving, i.e. connectivity of the mesh entities does not change. More precisely, as crack front nodes advance, mesh connectivity is invariant, and the crack surface extension splits the approximated material domain (see Fig. 3(a) and (b) in [72]). This leads to the aforementioned material configuration evolution and therefore to the discontinuity of $\varphi_i(X_I^{\mathrm{h}}, t)$. After each n_{steps} of propagation, mesh cutting is performed, which changes the mesh topology (see Fig. 3(c) in [72]).

Furthermore, we need to include certain mesh quality control, which will have immediate implications on the implementation of the virtual work contribution of traction and contact BCs, discussed in the following subsections. Note that mesh quality control is necessary since as crack propagates through a fixed mesh topology, some of the tetrahedrals adjacent to the crack front, $\partial \Gamma_{\mathrm{cr}}^{\mathrm{h}}$, are elongated while others are squashed. To overcome this issue, for each of the n_{steps} steps, quality control constraints are applied in a monolithic fashion to several layers of volume elements located around the crack front $\partial \Gamma_{\mathrm{cr}}^{\mathrm{h}}$ as presented in Fig. 5(b) and (c). This set of elements will be referred to as *smoothing bubble* and denoted by $\mathscr{S}_{\mathrm{B}}^{\mathrm{h}}$.

To account for the mesh quality control, a stabilising material force $f_I^{\mathrm{qual},m}$ is added to the system of equation and is defined as follows:

$$f_I^{\mathrm{qual},m} := \mathop{\mathbf{A}}_{\mathscr{S}_{\mathrm{B}}^{\mathrm{h}} \backslash \partial \Gamma_{\mathrm{cr}}^{\mathrm{h}}} \int_{\mathscr{S}_{\mathrm{B}}^{\mathrm{h}}} \frac{\partial M^m}{\partial \chi_\alpha} Q_{\alpha I}^{\mathrm{TET}} \mathrm{d}\Omega^{\mathrm{h}}, \tag{55}$$

where $Q_{\alpha I}^{\mathrm{TET}}$ represents a pseudo-stress at the tetrahedron-level and is defined as the counterpart of the first Piola–Kirchhoff stress, see [3]. This additional term operates solely in the material configuration and does not affect the solution of the crack propagation problem since no contribution is assembled to algebraic entries corresponding to crack front nodes.

4.2. Discretisation of boundary conditions when traversed by the crack front

In this section, the discretised versions of traction and contact boundary conditions for the case of crack propagation in the ALE formulation are presented.
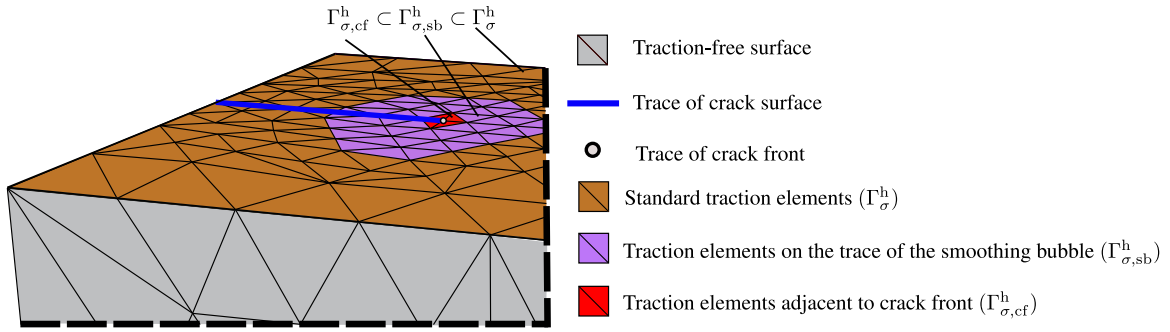
Fig. 6. Schematic presentation of traction elements in the ALE formulation for crack propagation.
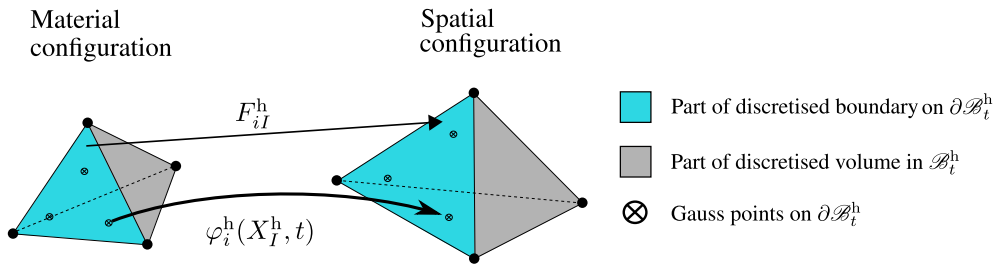

Fig. 7. Schematic presentation of the approximation of the deformation gradient tensor F_{iJ}^{h} on the element boundary.

4.2.1. Traction boundary conditions

The standard discretised version of the residual component for traction, $\mathscr{T}_i^{\mathrm{sp},s}$ is evaluated according to the expression $\delta\mathscr{T}^{\mathrm{sp}}$ in (44) as

$$\mathscr{T}_i^{\mathrm{sp},s} := \mathop{\mathbf{A}}_{\Gamma_\sigma^{\mathrm{h}}} \int_{\Gamma_\sigma^{\mathrm{h}}} S^s \bar{t}_i \mathrm{d}\Gamma^{\mathrm{h}}, \tag{56}$$

where $S^s \in H^1(\Gamma_{\mathrm{p}}^{\mathrm{h}})$ is a vector of n_{sp} basis functions for approximating spatial positions and $\bar{t}_i$ is the prescribed traction.

To the best of our knowledge, here, it is the first time that implicit consideration of the surface pressure boundary conditions is presented for crack propagation in ALE formulation. During the crack propagation analysis, the crack front can come close to or even traverse the surface where pressure is applied. To take this into account, an additional expression corresponding to $\delta\mathscr{T}^{\mathrm{mat}}$ in (44) has to be added to the residual vector:

$$\mathscr{T}_I^{\mathrm{mat},m} := - \mathop{\mathbf{A}}_{\partial\Gamma_{\mathrm{cr}}^{\mathrm{h}} \cap \Gamma_\sigma^{\mathrm{h}}} \int_{\Gamma_{\sigma,\mathrm{cf}}^{\mathrm{h}}} M^m F_{Ii} \bar{t}_i \mathrm{d}\Gamma^{\mathrm{h}}, \tag{57}$$

where $M^m \in H^1(\Gamma_\sigma^{\mathrm{h}})$ is a vector of n_{mat} basis functions for approximating material positions. The integration domain in (57) is represented by a single layer of triangular elements adjacent to the trace of the crack front $\partial\Gamma_{\mathrm{cr}}^{\mathrm{h}}$ on the traction surface $\Gamma_\sigma^{\mathrm{h}}$. Moreover, the assembly is performed only to the algebraic entry of the system associated with the single node corresponding to $\partial\Gamma_{\mathrm{cr}}^{\mathrm{h}} \cap \Gamma_\sigma^{\mathrm{h}}$, see Fig. 6. Since the material positions can change not only at the crack front but rather in the whole smoothing bubble (see Section 4.1.2), additional considerations will be required for a consistent linearisation of the residual components (56) and (57) on $\Gamma_{\sigma,\mathrm{sb}}^{\mathrm{h}}$, see details in Appendix A.

Furthermore, evaluation of F_{Ji}^{h} on the traction boundary requires a special technology for computing the trace of fields approximated in the volume at the Gauss points located on the surface of a tetrahedron, see Fig. 7. We implemented a technology similar to the one used in discontinuous Galerkin [81–83] and discontinuous Petrov–Galerkin [84,85] approaches. However, instead of evaluating volume quantities as traces on the mesh skeleton, here they are evaluated on the boundary of the mesh as it is also done for computing traction in the Nitsche method in
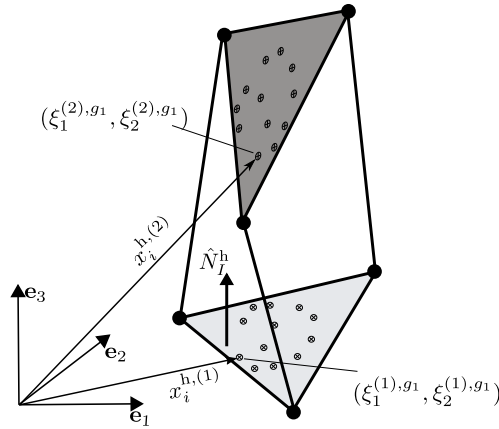
Fig. 8. Gap definition for non-matching meshes contact elements.

contact mechanics [86,87]. The consistent linearisation of the transpose of the deformation gradient tensor, F_{Ji}^{h}, is briefly discussed in Appendix B.

4.2.2. Coupling contact constraints with crack propagation in the ALE formulation

The mortar contact approach was chosen here for solving the problem of crack propagation along contact interfaces since it is an insignificantly variationally inconsistent approach [88]. Two types of face-to-face contact methods were considered: the standard mortar method for *non-matching meshes* and its special case for treating the case of *matching meshes*. As will be detailed below, the former, non-matching meshes contact approach is used for surfaces where crack will not pass while the latter, matching-meshes contact is considered for surfaces which the crack front can reach in the course of the propagation analysis.

To include the non-matching meshes contact, an approach similar to [38,39] was implemented to generate Gauss points between two overlapping triangles, one being on the slave surface and the other on the master surface. When two triangles overlap, a special contact prism is created that has no physical volume, i.e prisms are allowed to intersect. Each prism is then used to integrate the contact constrains on the triangular surfaces in the standard manner via clipping and triangulation procedure. However, since the developed framework is built using hierarchical base functions [80], which allow for spatially heterogeneous order of approximation, a non-standard approach has been chosen for evaluating the gap.

Commonly, the gap is evaluated at nodes of the slave side [38,39,78,89,90]. In this work, the gap is evaluated at each Gauss point of the slave side as the normal distance between a pair of Gauss points emerging from the clipping and the triangulation procedure. The approximated gap, $g_{\mathrm{con}}^{\mathrm{h}}$, between e.g. the first pair of Gauss points of the contact prism with coordinates $(\xi_1^{(1),g_1}, \xi_2^{(1),g_1})$ and $(\xi_1^{(2),g_1}, \xi_2^{(2),g_1})$ is computed as

$$g_{\mathrm{con}}^{\mathrm{h}}(x_i^{\mathrm{h},(1)}, x_i^{\mathrm{h},(2)}) = -\hat{N}_I^{\mathrm{h}} \delta_{iI}(x_i^{\mathrm{h},(1)} - x_i^{\mathrm{h},(2)}), \tag{58}$$

where superscript g_1 refers to the first Gauss point pair (see Fig. 8), and the unit normal $\hat{N}_I^{\mathrm{h}}$ is computed as was shown in (53). The evaluation of the Gauss point-wise gap permits to consider gap-related quantities corresponding to a single contact element when performing numerical integration, in contrast to the commonly used node-wise weighted gap evaluated as a mean of contributions from all elements adjacent to a node on the contact surface [39].

When one of the contacting surfaces is traversed by the trace of the crack front, triangles located on the surface cut by the crack will move in the material domain with respect to the triangles located on the intact contact surface. Furthermore, material displacements arising from crack extension and mesh quality improvement can be large even if the spatial displacements are assumed small. In such cases, consistent integration of contact pressure on both sides of the contact interface can be achieved by convecting the contact Gauss points [39,78]. However, this would necessitate linearisation of the Gauss point coordinates generated by the clipping procedure, in addition to coupled KKT conditions of contact (39) and Griffith criterion (32) in this framework. Therefore, we propose here a more suitable approach, utilising the ALE formulation to preserve the "shadowing" of contact elements originally placed
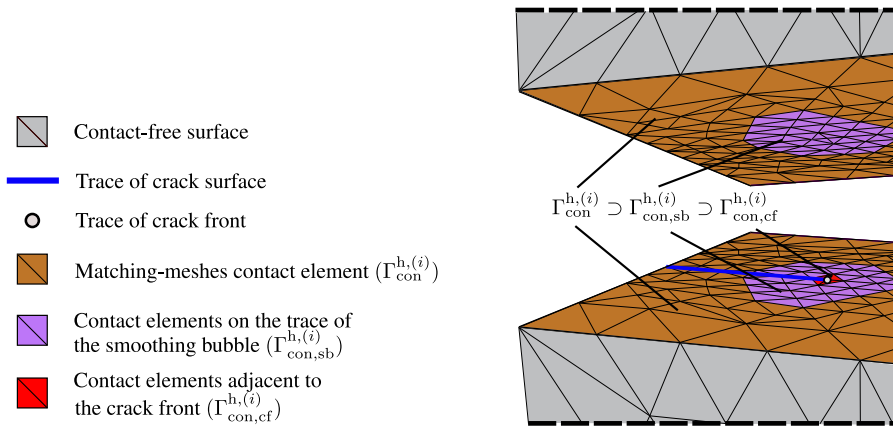
Fig. 9. Schematic presentation of matching-meshes contact elements in the ALE crack propagation formulation.

on top of each other in the material configuration, which we will refer to as the matching meshes contact. This can be achieved by imposing a simple constraint on the material positions of nodes of the contact interface, enforcing nodes of the intact surface to follow the nodes of the cut surface in the material domain, as will be shown below.

In the current approach, in order to generate matching meshes on the potential contact surfaces, the bodies are initially meshed having common vertices, edges and faces along matching-meshes contact interfaces. Thereafter, the meshes are disconnected by replacing the common triangles of the two meshed bodies with zero volume prism elements where one triangle is part of the master body and the other triangle is part of the slave. Hence, in the matching-meshes case prisms are not overlapping and therefore no clipping is needed since the triangles of the two prisms sides are fully coinciding in the reference configuration. Nevertheless, the gap evaluation is performed in exactly the same fashion as for non-matching meshes contact presented in Eq. (58).

A schematic of two meshed bodies where only one is cracked is presented in Fig. 9. The bodies are in contact but are shown separated for visual clarity. The triangular faces are coinciding, and there are edges not shown here connecting the matching vertices located on the two separate faces. It should be noted that the contact elements adjacent to the crack front, $\Gamma_{\mathrm{con,cf}}^{h,(i)}$, are present only on the one of the contacting surfaces since the crack front is located only on one of the two bodies coming into contact. However, the rest of the elements of $\Gamma_{\mathrm{con}}^{h,(i)}$ and $\Gamma_{\mathrm{con,sb}}^{h,(i)}$ are located on both sides of the contact surface. It must be clarified also that for contact surfaces where crack is not expected to pass, non-matching meshes mortar contact is applied.

The common formulation of both matching and non-matching meshes contact elements includes the residual components associated with the contact traction on slave $\mathscr{Q}_i^{(1),s}$ and master $\mathscr{Q}_i^{(2),s}$ sides and with the contact complementarity constraint $\mathscr{C}_{\mathrm{con}}^c$, following contributions in Eqs. (45) and (46):

$$\mathscr{Q}_i^{(1),s} := \underset{\Gamma_{\mathrm{con}}^{h,(1)}}{\mathbf{A}} \int_{\Gamma_{\mathrm{con}}^{h,(1)}} S^s \hat{N}_J \delta_{iJ} \lambda^h \mathrm{d}\Gamma^h, \quad \mathscr{Q}_i^{(2),s} := - \underset{\Gamma_{\mathrm{con}}^{h,(2)}}{\mathbf{A}} \int_{\Gamma_{\mathrm{con}}^{h,(2)}} S^s \hat{N}_J \delta_{iJ} \lambda^h \mathrm{d}\Gamma^h,$$

$$\mathscr{C}_{\mathrm{con}}^c := \underset{\Gamma_{\mathrm{con}}^{h,(1)}}{\mathbf{A}} \int_{\Gamma_{\mathrm{con}}^{h,(1)}} \Lambda^c C_{\mathrm{con}}^h \mathrm{d}\Gamma^h, \tag{59}$$

where $\lambda^h = \sum_{c=1}^{n_\lambda} \Lambda^c \tilde{\lambda}^c$ is the approximated Lagrange multipliers scalar field and C_{con}^h is the approximated complementarity function (40) defined as:

$$C_{\mathrm{con}}^h := \lambda^h - \max\left(0, \lambda^h - c_n g^h\right), \tag{60}$$

with $S^s \in H^1\left(\Gamma_{\mathrm{con}}^{h,(i)}\right)$, $\Lambda^c \in H^1\left(\Gamma_{\mathrm{con}}^{h,(i)}\right)$ and $\tilde{\lambda}^c$ being contact Lagrange multiplier DOFs.

The residual contribution of the additional virtual work term presented in (47) is evaluated either on the master or the slave side depending on where the trace of the crack front lies, and is expressed as:

$$\mathscr{R}_I^{(i),m} = (-1)^i \mathop{\textbf{A}}_{\partial\Gamma_{cr}^h \cap \partial\Gamma_{con,cf}^{h,(i)}} \int_{\Gamma_{con,cf}^{h,(i)}} M^m \lambda^h F_{Ji} \hat{N}_J \delta_{iI} d\Gamma^h, \tag{61}$$

where $i = 1$ if the slave body is cracked and $i = 2$ otherwise.

Since material positions can change in the whole smoothing bubble (see Section 4.1.2), additional considerations will be required for a consistent linearisation of the residual components (59) and (61) on $\Gamma_{con,sb}^h$. The treatment of these components will be similar to the linearisation of the terms (56) and (57) discussed in Section 4.2.1, see details in Appendix C.

To ensure the "shadowing" of the contact elements on the cut contact surface by the corresponding elements on the intact surface, an additional constraint can be added on the relatively small number of material nodes located on $\Gamma_{con,sb}^{h,(i)}$. The constraint is then imposed via a set of vectorial Lagrange multipliers $\tilde{\lambda}_I^{mat}$ enforcing the nodes on the intact surface side to follow the corresponding shadowed nodes on the cracked body surface. Therefore, the extra residual contributions from the constraints on material nodes read:

$$\mathscr{N}_I^m := \tilde{\lambda}_I^{mat,m} \text{ on } \Gamma_{con,sb}^{(\eta)} \quad \text{and} \quad r_I^{\lambda mat,h,w} := [\tilde{X}_I^{(\eta)} - \tilde{X}_I^{(\eta')}]^w \quad \text{on } \Gamma_{con,sb}^{(\eta)}, \tag{62}$$

where (η) denotes the intact surface and (η') denotes the cracked surface.[1]

4.3. Constraints for crack propagation

The residual contribution from the KKT conditions for Griffith's criterion (43) is implemented in the nodal sense since the first order approximation is adapted for material positions:

$$\mathscr{C}_{cr}^q := \mathop{\textbf{A}}_{\partial\Gamma_{cr}^h} C_{cr}(\tilde{\rho}^q, \tilde{X}_I^q), \tag{63}$$

where $C_{cr}(\tilde{\rho}^q, \tilde{X}_I^q)$ is the nodal value of (43).

4.4. Constraints for shape preservation

In [3], the shape-preserving constraints were enforced on the boundaries intersected by the smoothing bubble (i.e. on $\partial\mathscr{B}_t^h \cap \partial\mathscr{S}_B^h$) via additional Lagrange multipliers field β. Here, the associated residuals are presented for the sake of completeness:

$$\mathscr{O}_I^m := \mathop{\textbf{A}}_{\partial\mathscr{B}_t^h \cap \partial\mathscr{S}_B^h} \int_{\partial\mathscr{S}_B^h} \beta^h \hat{N}_I^h M^m d\Gamma^h, \quad r_{sh}^v := \mathop{\textbf{A}}_{\partial\mathscr{B}_t^h \cap \partial\mathscr{S}_B^h} \int_{\partial\mathscr{S}_B^h} B^v \hat{N}_I^h (X_I^h - \chi_\alpha^h \delta_{\alpha I}) d\Gamma^h, \tag{64}$$

where $\beta^h := \sum_{v=0}^{B_{tot}} B^v \tilde{\beta}^v$ is the approximated field for shape-preserving Lagrange multipliers, with $B^v \in H^1(\partial\mathscr{B}_t^h \cap \partial\mathscr{S}_B^h)$ being the shape functions for β field and $\tilde{\beta}^v$ being the associated DOFs.

4.5. Monolithic solution via arc-length control

At each step of the crack propagation analysis, the linearised system of equations is solved to fulfil global equilibrium in a monolithic fashion, i.e. as a fully coupled problem by means of the Newton–Raphson method. The arc-length control was adopted to control crack propagation by constraining the crack surface to monotonically increase at each step by a prescribed amount. This is expressed through the following residual:

$$r^{arc,\tau} := \sum_{c=1}^{n_{fr}} \tilde{A}_I^{\partial\Gamma_{cr},c} \left(\left[\tilde{X}_I^c\right]^t - \left[\tilde{X}_I^c\right]^{t-1} \right) - \Delta A^{h,\Gamma_{cr}}, \tag{65}$$

---

[1] In addition to the constraints for preserving shadowing of contact elements, we also use similar constraints to tie material positions of the nodes of triangles lying on the two crack surfaces. This is done since a unique definition of the discretised crack surface in material configuration is required for mesh cutting.

Table 1

List of fields in the coupled problem and the associated DOFs and basis functions.

Field names	DOF symbols	Basis function symbols
Spatial positions	$\tilde{x}_i$	S
Material positions	$\tilde{X}_I$	M
LM for contact constraints	$\tilde{\lambda}$	Λ
LM for shape preservation	$\tilde{\beta}$	B
LM for matching-mesh contact "shadowing" preservation	$\tilde{\lambda}^{\mathrm{mat}}$	node-based
LM for crack front extension	$\tilde{\rho}$	node-based
LM for arc length	$\tilde{\tau}$	not approximated field

where $\tilde{A}_I^{\partial\Gamma_{\mathrm{cr}},c}$ is defined in (52), $\Delta A^{\mathrm{h},\Gamma_{\mathrm{cr}}}$ is the area increment prescribed for the arc-length control scheme, n_{cf} is the number of nodes on $\partial\Gamma_{\mathrm{cr}}^{\mathrm{h}}$, superscript t stands for the current step and $t-1$ for the previous one.

4.6. Linearised system of equations

In Table 1 we collected all DOF and basis function symbols used to approximate various field appearing in the coupled problem. To present the linearised system of equations, first the residuals for the spatial positions and material positions are defined below:

$$
\begin{aligned}
r_i^{\mathrm{sp},s} &:= f_i^{\mathrm{sp},s} + \tilde{\tau}\,\mathscr{T}_i^{\mathrm{sp},s} + \mathscr{Q}_i^{(1),s} + \mathscr{Q}_i^{(2),s}, \\
r_I^{\mathrm{mat},m} &:= \tilde{\tau}\,\mathscr{T}_I^{\mathrm{mat},m} + \mathscr{F}_I^m + \mathscr{N}_I^m + \mathscr{M}_I^m + f_I^{\mathrm{qual},m} + \mathscr{R}_I^{(i),m} + \mathscr{O}_I^m.
\end{aligned}
\tag{66}
$$

The linearised system of equation for the coupled problem reads:

$$
\begin{bmatrix}
\dfrac{\partial f_i^{\mathrm{sp},s}}{\partial \tilde{x}_j} & \dfrac{\partial r_i^{\mathrm{sp},s}}{\partial \tilde{X}_J} & \dfrac{\partial \mathsf{A}_i^s}{\partial \tilde{\lambda}} & \mathbf{0} & \mathbf{0} & \mathbf{0} & \mathscr{T}_i^{\mathrm{sp},s} \\[2mm]
\dfrac{\partial \mathsf{B}_I^m}{\partial \tilde{x}_j} & \dfrac{\partial \mathsf{C}_I^m}{\partial \tilde{X}_J} & \dfrac{\partial \mathscr{R}_I^{(i),m}}{\partial \tilde{\lambda}} & \dfrac{\partial \mathscr{O}_I^m}{\partial \tilde{\beta}} & \dfrac{\partial \mathscr{N}_I^m}{\partial \tilde{\lambda}_J^{\mathrm{mat}}} & \dfrac{\partial \mathscr{M}_I^m}{\partial \tilde{\rho}} & \mathscr{T}_I^{\mathrm{mat},m} \\[2mm]
\dfrac{\partial \mathscr{C}_{\mathrm{con}}^c}{\partial \tilde{x}_j} & \dfrac{\partial \mathscr{C}_{\mathrm{con}}^c}{\partial \tilde{X}_J} & \dfrac{\partial \mathscr{C}_{\mathrm{con}}^c}{\partial \tilde{\lambda}} & \mathbf{0} & \mathbf{0} & \mathbf{0} & \mathbf{0} \\[2mm]
\mathbf{0} & \dfrac{\partial r_I^{\lambda^{\mathrm{mat,h}},w}}{\partial \tilde{X}_J} & \mathbf{0} & \mathbf{0} & \mathbf{0} & \mathbf{0} & \mathbf{0} \\[2mm]
\mathbf{0} & \dfrac{\partial \mathscr{C}_{\mathrm{cr}}^q}{\partial \tilde{X}_J} & \mathbf{0} & \mathbf{0} & \dfrac{\partial \mathscr{C}_{\mathrm{cr}}^q}{\partial \tilde{\rho}} & \mathbf{0} & \mathbf{0} \\[2mm]
\mathbf{0} & \dfrac{\partial r_{\mathrm{sh}}^v}{\partial \tilde{X}_J} & \mathbf{0} & \mathbf{0} & \mathbf{0} & \mathbf{0} & \mathbf{0} \\[2mm]
\mathbf{0} & \dfrac{\partial r^{\mathrm{arc},\tau}}{\partial \tilde{X}_J} & \mathbf{0} & \mathbf{0} & \mathbf{0} & \mathbf{0} & \mathbf{0}
\end{bmatrix}
\begin{bmatrix}
\Delta \tilde{x}_i \\
\Delta \tilde{X}_I \\
\Delta \tilde{\lambda} \\
\Delta \tilde{\lambda}^{\mathrm{mat}} \\
\Delta \tilde{\rho} \\
\Delta \tilde{\beta} \\
\Delta \tilde{\tau}
\end{bmatrix}
= -
\begin{bmatrix}
r_i^{\mathrm{sp},s} \\
r_I^{\mathrm{mat},m} \\
\mathscr{C}_{\mathrm{con}}^c \\
r_I^{\lambda^{\mathrm{mat,h}},w} \\
\mathscr{C}_{\mathrm{cr}}^q \\
r_{\mathrm{sh}}^v \\
r^{\mathrm{arc},\tau}
\end{bmatrix},
\tag{67}
$$

where the sums appearing on the left-hand side are denoted as:

$$
\begin{aligned}
\mathsf{A}_i^s &:= \mathscr{Q}_i^{(1),s} + \mathscr{Q}_i^{(2),s} \\
\mathsf{B}_I^m &:= \tilde{\tau}\,\mathscr{T}_I^{\mathrm{mat},m} + \mathscr{F}_I^m + \mathscr{R}_I^{(i),m} \\
\mathsf{C}_I^m &:= \tilde{\tau}\,\mathscr{T}_I^{\mathrm{mat},m} + \mathscr{F}_I^m + \mathscr{M}_I^m + f_I^{\mathrm{qual},m} + \mathscr{R}_I^{(i),m} + \mathscr{O}_I^m,
\end{aligned}
\tag{68}
$$

and the components of the vector with Δ symbol represent increments of the unknown values on an iteration of a non-linear solver.
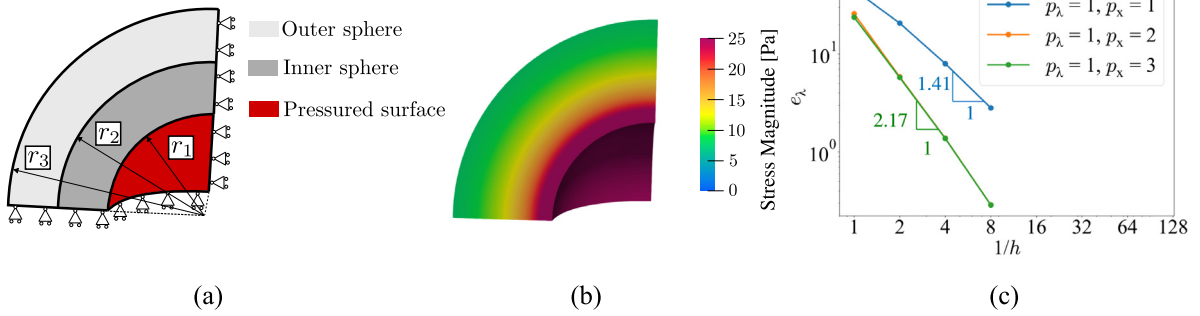
Fig. 10. Matching-meshes contact verification: (a) schematic of one-eighth of two hollow conforming spheres coming into contact due to pressure p on the inner surface of the inner sphere (see input parameters in Table 2), (b) radial stress distribution and (c) L^2 error of contact pressure with decreasing mesh element size h.

The proposed framework was entirely developed using the open source finite element software MoFEM[2] [91] which integrates the open source libraries PETSc (Portable, Extensible Toolkit for Scientific Computation) [92] and MOAB [93]. The system of equations presented in   is solved using routines available with PETSc package in a parallel distributed-memory environment. Furthermore, the mesh-oriented database MOAB is used to process mesh data and perform all operations for mesh cutting and matching-meshes/non-matching-meshes contact prisms generation presented in Sections 4.1.2 and 4.2.2, respectively.

5. Numerical examples

In this section, several numerical examples are presented to verify the model formulation and implementation, and to highlight the effect of surface traction on the crack propagation process. The robustness of the developed approach is validated by comparison with previous numerical results and with experimental data for a civil nuclear industry application which involves a crack of complex morphology propagating along contact interfaces between multiple deformable bodies. Input mesh files, parameter files and output files for examples considered in Sections 5.4–5.6 and crack propagation animations for the industrial application discussed in Section 5.6 are available in the Supplementary material [94].

5.1. Verification of contact formulation

We verify matching-meshes contact element implementation with hierarchical base functions by analysing results for a problem involving conforming contact interface between two hollow spheres, see Fig. 10. Pressure p is applied on the inner surface of the inner sphere. The numerical solution is compared with an analytical formula for radial stress, σ_{rr}, that is:

$$\sigma_{rr}(r) = \frac{r_1^3}{r_3^3 - r_1^3} \frac{r_3^3 - r^3}{r^3} p, \tag{69}$$

where r_1 and r_3 are the inner radius of the inner sphere and the outer radius of the outer sphere, respectively.

The L^2 error of the pressure on the contact surface Γ_{con}^h at $r = r_2$ is evaluated as:

$$e_\lambda := \left(\int_{\Gamma_{con}^h} (\sigma_{rr}(r) - \lambda^h)^2 d\Gamma^h \right)^{1/2}, \tag{70}$$

where λ^h is the value of the contact Lagrange multipliers field.

---

[2] The source codes of the implementation of the proposed framework can be found in the three following repositories: https://bitbucket.org/likask/mofem-cephas/src/Version0.14.0 (MoFEM core library), https://bitbucket.org/likask/mofem_um_fracture_mechanics/src/Version0.14.0 (fracture mechanics module) and https://bitbucket.org/mofem/mortar_contact/src/Version0.14.0 (mortar contact module). The version of the code used to obtain results presented in Section 5 can be installed through Spack package manager (https://spack.io) by running terminal command `spack install mofem-fracture-module@0.14.0` (see http://mofem.eng.gla.ac.uk for installation instructions).

Table 2
Input parameters used for two hollow spheres contact test (matching-meshes).

r_1 [m]	r_2 [m]	r_3 [m]	E [Pa]	ν	p [Pa]
40	30	20	2000	0.3	25

Table 3
Input parameters used for Hertz contact test (non-matching-meshes).

E_1 [Pa]	ν_1	E_2 [Pa]	ν_2	R [m]	P [N]	p [Pa]
10^3	0.4	10^4	0.2	20	0.0712	0.0178

(a)   (b)   (c)
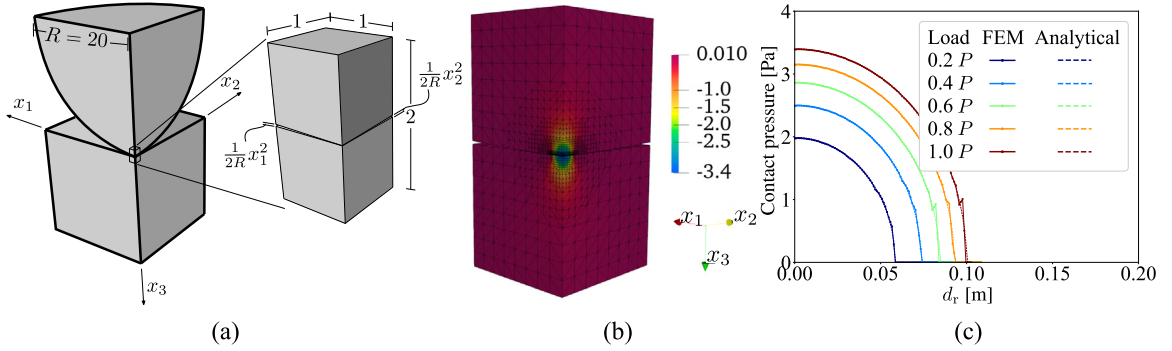
Fig. 11. Verification for non-matching-meshes contact (Hertz problem), see input in Table 3: (a) schematic of one-eighth of a deformable sphere coming into contact with a deformable cube due to applied pressure p on the top of the eighth-sphere; a zoom-in at the vicinity of sphere's apex in contact with the flat surface of the cube that is the actual problem solved, (b) vertical stress distribution for the problem solved at $1.0P$ and (c) comparison between analytical and numerical solutions for the problem.

Results are presented in Fig. 10(c) for three combinations of contact Lagrange multipliers approximation order, p_λ, and spatial positions approximation order p_x. Approximation order p_λ is kept equal to unity based on the findings of [95], where it was presented that higher order basis for Lagrange multipliers in $H^1(\Gamma_{con}^h)$ space can result in spurious oscillations. Furthermore, linear mesh geometry was used for all analyses. A significant increase in convergence rate can be observed for order increment between $p_x = 1$ and $p_x = 2$, explained by sheer locking for the 1st order of approximation, however, no change is observed between $p_x = 2$ and $p_x = 3$.

Non-matching-meshes contact is verified by analysing contact between a deformable sphere and deformable body with flat surface (see Fig. 11). The results are compared to the analytical Hertz solution, according to which the effective Young's modulus, E^*, the maximum contact pressure $p_{c,max}$ and the radius of the contact area, a, are defined as [96]:

$$E^* = \frac{E_1 E_2}{(1 - \nu_1^2)E_2 + (1 - \nu_2^2)E_1}, \quad p_{c,max} = \left(\frac{6PE^{*2}}{\pi^3 R^2}\right)^{1/3}, \quad a = \left(\frac{3PR}{4E^*}\right)^{1/3}, \tag{71}$$

where P is the total load applied to the deformable sphere. The subscripts 1 and 2 refer to material parameters for sphere and cube, respectively. For the quarter problem presented in Fig. 11(a) the load P is uniformly applied to the upper flat surface of unit area as $P/4$. All input parameters are presented in Table 3. For this problem, contact pressure profile $p_c(d_r)$ is expressed as:

$$p_c(d_r) = p_{c,max}\sqrt{1 - (d_r/a)^2}, \tag{72}$$

where d_r is the radial distance from the centre of the contact area.

Numerical results coincide with the analytical solution everywhere except for the vicinity of the boundary between contact and non-contact zones, where oscillations of the contact pressure are observed, see Fig. 11(c). Note that such oscillations of contact pressure at the boundaries of contact zones are typical for mortar-based formulations which use continuous approximation of contact pressure, see e.g. [38] and discussions in [97]. At the
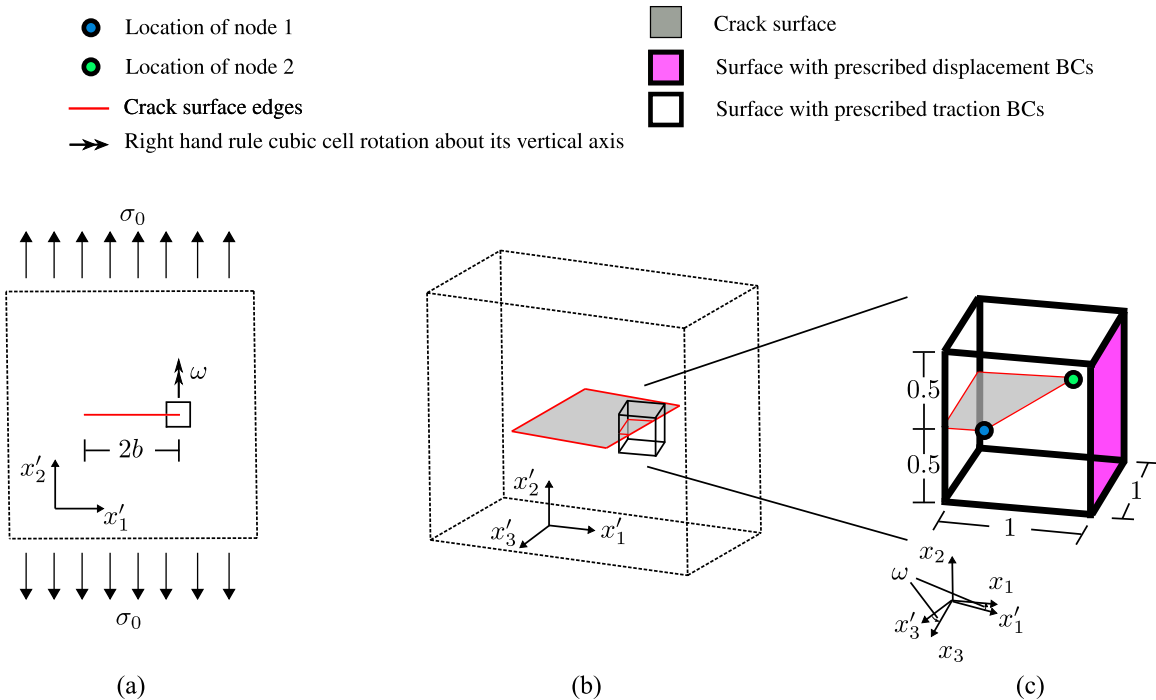
Fig. 12. Schematic of the problem setup for verification of the traction term in the material domain (57): (a) 2D schematic of an infinite body under plane strain conditions with a crack of length $2b$ and far-field normal traction σ_0; a unit cube is considered having faces aligned with x'_1, x'_2, x'_3 coordinate system, the crack surface penetrates the cube until its centre; (b) 3D schematic of the same plate with unit cube rotated anticlockwise by angle ω about x'_2 axis; (c) zoom-in view of the unit cube after rotation where one face has displacement BCs prescribed and the rest of the faces have traction BCs prescribed; locations of two crack front nodes on cube's faces are highlighted.

same time, due to their localisation, these oscillations do not have any significant effect in applications considered below, and, therefore, the $H^1(\Gamma^{\mathrm{h}}_{\mathrm{con}})$ approximation of contact Lagrange multipliers was deemed acceptable for the present work. However, we note that these oscillations can be avoided if dual approximation of Lagrange multipliers is used [37,39], or, more generally, if the contact pressure is approximated in $H^{-1/2}(\Gamma^{\mathrm{h}}_{\mathrm{con}})$ space. Such modification of the present framework is the subject of future work.

5.2. Verification of the crack energy release rate on a surface under load

In this section, we verify the implementation of the virtual work of surface traction in the material domain, i.e. of the term $\mathscr{T}^{\mathrm{mat}}$ in (44) (see (57) for the discretised setting), which contributes to configurational forces driving crack propagation. The verification is based on comparison of the crack energy release rate computed in simulation and from an analytical solution for the stress state around the crack tip in an infinite body under plane strain conditions [98], see Fig. 12(a). Since in the analytical solution the tangential traction is equal to zero on any surface perpendicular to the crack front, we consider a unit cube originally aligned with the crack surface and then rotated anticlockwise by an angle ω about the x'_2 axis. As a result of this rotation, the crack front is inclined by angle ω with respect to two surfaces of the rotated cube, see Fig. 12(b); therefore, both normal and tangential traction components are non-zero on cube's surfaces intersected by the crack front.

For the case when the Poisson's ratio $\nu = 0$, the traction components on cube's surfaces after the rotation can be computed as:

$$
\begin{bmatrix} t_1 \\ t_2 \\ t_3 \end{bmatrix} = \begin{bmatrix} \sigma_1 \cos^2(\omega) & \tau_{12} \cos(\omega) & \sigma_1 \sin(\omega)\cos(\omega) \\ \tau_{12} \cos(\omega) & \sigma_2 & \tau_{12} \sin(\omega) \\ \sigma_1 \sin(\omega)\cos(\omega) & \tau_{12} \sin(\omega) & \sigma_1 \sin^2(\omega) \end{bmatrix} \begin{bmatrix} n_1 \\ n_2 \\ n_3 \end{bmatrix},
\tag{73}
$$

where n_1, n_2 and n_3 are the components of the unit normal vector to the surfaces of the rotated cube. The stress components σ_1, σ_2 and τ_{12} are evaluated according to the original solution as:

$$
\begin{aligned}
\sigma_1 &= \frac{K_I}{\sqrt{2\pi r}} \cos\frac{\theta}{2} \left(1 - \sin\frac{\theta}{2}\sin\frac{3\theta}{2}\right), \\
\sigma_2 &= \frac{K_I}{\sqrt{2\pi r}} \cos\frac{\theta}{2} \left(1 + \sin\frac{\theta}{2}\sin\frac{3\theta}{2}\right), \\
\tau_{12} &= \frac{K_I}{\sqrt{2\pi r}} \sin\frac{\theta}{2}\cos\frac{\theta}{2}\cos\frac{3\theta}{2},
\end{aligned}
\tag{74}
$$

where $K_I = \sigma_0\sqrt{\pi b}$ is the Mode-I stress intensity factor, while the radial distance from the crack front r and the polar angle θ in the original coordinate plane $x_1' x_2'$ are evaluated as:

$$
\theta(x_1, x_2, x_3) = \tan^{-1}\left(\frac{x_2}{x_1\cos(\omega) + x_3\sin(\omega)}\right), \quad r(x_1, x_2, x_3) = \sqrt{(x_1\cos(\omega) + x_3\sin(\omega))^2 + x_2^2}.
\tag{75}
$$

In the verification analysis, traction boundary conditions (73) are prescribed on all surfaces of the cube except for the surface opposite to the fully cracked one (see Fig. 12(c)), where displacement boundary conditions are defined according to the analytical solution [98]:

$$
\begin{aligned}
x_1 - X_1 &= K_I \frac{1+\nu}{E} \left(\frac{r(X_1, X_2, X_3)}{2\pi}\right)^{1/2} \cos\frac{\theta}{2}(3 - 4\nu - \cos\theta)\cos(\omega), \\
x_2 - X_2 &= K_I \frac{1+\nu}{E} \left(\frac{r(X_1, X_2, X_3)}{2\pi}\right)^{1/2} \sin\frac{\theta}{2}(3 - 4\nu - \cos\theta), \\
x_3 - X_3 &= K_I \frac{1+\nu}{E} \left(\frac{r(X_1, X_2, X_3)}{2\pi}\right)^{1/2} \cos\frac{\theta}{2}(3 - 4\nu - \cos\theta)\sin(\omega).
\end{aligned}
\tag{76}
$$

The verification test does not require the crack propagation analysis since nodal values of crack energy release rate, G^n, can be understood as values of nodal Lagrange multipliers that prevent the crack area change. The constraints for crack area change can be expressed as:

$$
\sum_{m=1}^{n_{\text{fr}}} \sum_{J=1}^{3} C_{IJ}^{nm}\left(\tilde{X}_J^m - \tilde{\chi}_J^m\right) = \{0\}, \qquad C_{IJ}^{nm} = \delta^{nm}\delta_{IJ}\tilde{A}_J^{\partial\Gamma_{\text{cr}}, m} \quad \text{(no summation on m and J)},
\tag{77}
$$

where $\tilde{A}_J^{\partial\Gamma_{\text{cr}}, m}$ was defined in (52) and δ^{mn} and δ_{IJ} are Kronecker delta functions. Constraints presented in (77) can be expressed using a $3n_{\text{fr}} \times 3n_{\text{fr}}$ matrix of the following form:

$$
\mathbf{C} = C_{IJ}^{nm}.
\tag{78}
$$

Following Ainsworth [99], the crack energy release rate at crack front nodes can be computed as:

$$
\mathbf{G}^{\text{front}} = \left[\mathbf{C}^{\text{T}}(\mathbf{C}\mathbf{C}^{\text{T}})^{-1}\right]^{\text{T}}\mathbf{f}^{\text{mat}},
\tag{79}
$$

where $\mathbf{G}^{\text{front}}$ stands for the vector of G^n and $\mathbf{f}^{\text{mat}}$ refers to the vector notation of $\mathscr{F}_J^m + \mathscr{T}_J^{\text{mat},m}$ which is the sum of the terms presented in (50) and (57).

It should be noted that the constraint (77) is not added to the system of equations when solving the problem, but is used as post-processing means to compute crack energy release rate at crack front nodes. The units of the elements of $\mathbf{C}$ matrix are [m^2] and the units of the elements of the vector $\mathbf{f}^{\text{mat}}$ are [Nm], hence the units [N/m] are preserved for G^{h}. Furthermore, in this test we used tetrahedral [100] and triangular [101,102] quarter-point elements for integration in the volume around the crack front and on traction surfaces, respectively. These elements provide the appropriate approximation of the singularity in stress and strain fields, increasing the precision of the stress intensity factor computation, see [72] for more details.

Parameters for the verification test are presented in Table 4, where E is Young's modulus, ν is Poisson's ratio, p_{g} stands for the order of approximation for spatial positions used globally, while p_{r} refers to the order of approximation locally increased in the vicinity of the crack front (as a result of hp-refinement) where a higher accuracy is

Table 4
Parameters for verification of material traction term.

E [N/m^2]	K_I [N/m$^{3/2}$]	ν	G_{ref} [N/m]	ω [rad]	p_g	p_r
10^5	1	0	10^{-5}	$\pi/5$	2	3

Table 5
Relative error of approximated crack energy release rate with full term (57) considered, without the normal or the tangential traction contributions to the virtual work in the material domain, and without the term (57) completely. The error is evaluated at the crack front nodes 1 and 2 as presented in Fig. 12.

Relative error (80)	With full (57)	w/o normal part of (57)	w/o tangent part of (57)	w/o (57)
e_{G^h} node 1	2.9×10^{-2}	3.33×10^1	5.639×10^3	0.5672×10^4
e_{G^h} node 2	1.92×10^{-2}	0.6308×10^1	1.3631×10^4	1.3677×10^4

Table 6
Input parameters for analyses with setup presented in Fig. 13.

g_{cr} [N/mm]	E_{gr} [N/m^2]	ν_{gr}	p_g	p_r
0.23	10.9×10^9	0.2	2	4

needed [72], and $G_{ref} = K_I^2 E$ is the analytical crack energy release rate. The relative error of approximated G^h value at nodes 1 and 2 (see Fig. 12) is evaluated as:

$$e_{G^h} = \left| \frac{G^h - G_{ref}}{G_{ref}} \right|. \tag{80}$$

The verification results are presented in Table 5. It can be observed that when the full contribution of the term (57) is considered, the relative error of the numerical result is below 3% for both nodes of the crack front trace, which is satisfactory and can be further decreased with mesh refinement. However, if the normal part of (57) is omitted in the formulation, the error increases by 3 orders of magnitude. Furthermore, when the contribution of the tangential traction in the material domain is omitted, the error increases by 3 more orders of magnitude, highlighting the more pronounced effect of the tangential component of traction on the crack energy release rate computation. It should be noted though that for the rest of the nodes along the crack front, the relative error of G^h is not significant in both presence and absence of (57).

5.3. Importance of consistent formulation of traction for crack propagation

According to the example presented in Section 5.2, the absence of material forces term (57) results in high errors of the crack energy release rate G at the trace of the crack front on surfaces with traction. In this section, we investigate further the effect of the material traction term on crack propagation.

For this, a comparison is performed of two crack propagation analyses of thin plate subjected to tangential traction on the cracked surface (Fig. 13): in the absence and in the presence of the surface traction term (57). The input parameters are presented in Table 6. The plate was chosen to be thin to reduce the influence of the material forces arising in the volume and increase the importance of the material traction on the crack front trace. Note that we did not use in the propagation analysis the quarter-point element mentioned in Section 5.2, since in previous work it was shown that while this element improves the precision of computed crack energy release rate, it does not have any significant effect on the crack propagation process [72].

The final crack surface for each case is presented in Fig. 14. For the case where term (57) is absent, the crack has extended predominantly on one side which impedes the propagation analysis as seen in Fig. 14(a). As presented in Section 5.2, the absence of (57) results in high errors of G at the trace of the crack front on surfaces with tangential traction. Therefore, the overestimation of G drives the crack front to propagate predominantly on one side of the plate which is a non-physical behaviour. This result highlights the importance of considering the effect of tangential traction acting on the end of the crack front. Such situation is naturally appearing when considering crack traversing a contact interface with friction taken into account, which is not studied in the present paper but is the topic of future work.
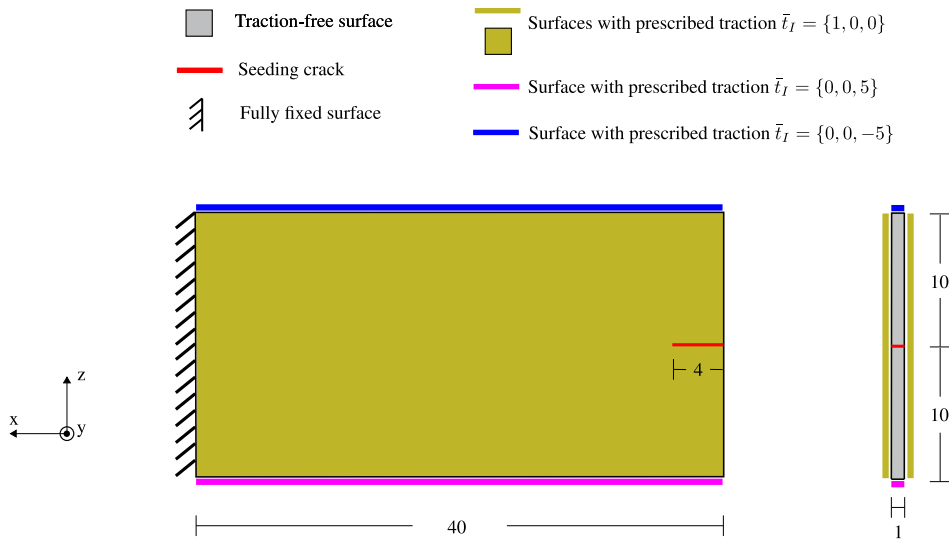
Fig. 13. Schematic of thin plate with seeded notch subject to tangential traction on cracked surface and normal traction applied on the horizontal faces opening the crack.
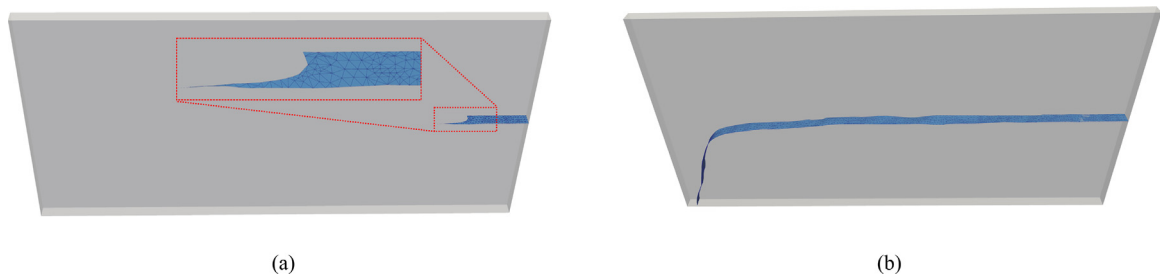

(a)   (b)

Fig. 14. Last step for crack propagation analysis with BCs presented in Fig. 13: (a) excluding (with a zoom-in of the crack surface) and (b) including (57).

On the other hand, when the term (57) is considered in the formulation, the error in the crack energy release rate is significantly reduced and the crack propagates, on average, symmetrically on both sides until the plate is fully cracked as presented in Fig. 14(b). It should be noted also that despite the symmetry of the loading, the crack propagated towards the bottom face of the plate as the crack path can bifurcate due to numerical errors.

5.4. Validation of integration of contact formulation within the crack propagation framework

Numerical analyses of fracture of a graphite cylinder slice (see Fig. 15) previously presented in [3] are used here to validate the integration of contact model within the ALE crack propagation framework. The original results involved modelling the interface between graphite and steel components by tied meshes i.e. by having both normal and tangential traction transferred between the two bodies. In this work, we compare results for tied mesh and solutions with contact formulation for matching and non-matching contact interfaces. The material input parameters used in these analyses (presented in Table 7 with E_{st} and ν_{st} being the steel components Young's modulus and Poisson's ratio, respectively) and the geometry of the mesh are the same as those presented in [3]. Furthermore, the global order of approximation of spatial positions $p_g = 2$, while the increased order $p_r = 3$ which provides a sufficient accuracy for this problem [3].

Comparison of curves of elastic energy versus crack area is presented in Fig. 16(a) for the three aforementioned analyses of non-matching, matching and tied meshes and the tied mesh presented in [3] for Order-2 as corrected in [103]. It can be seen that the results of the present framework for tied mesh almost coincide with that
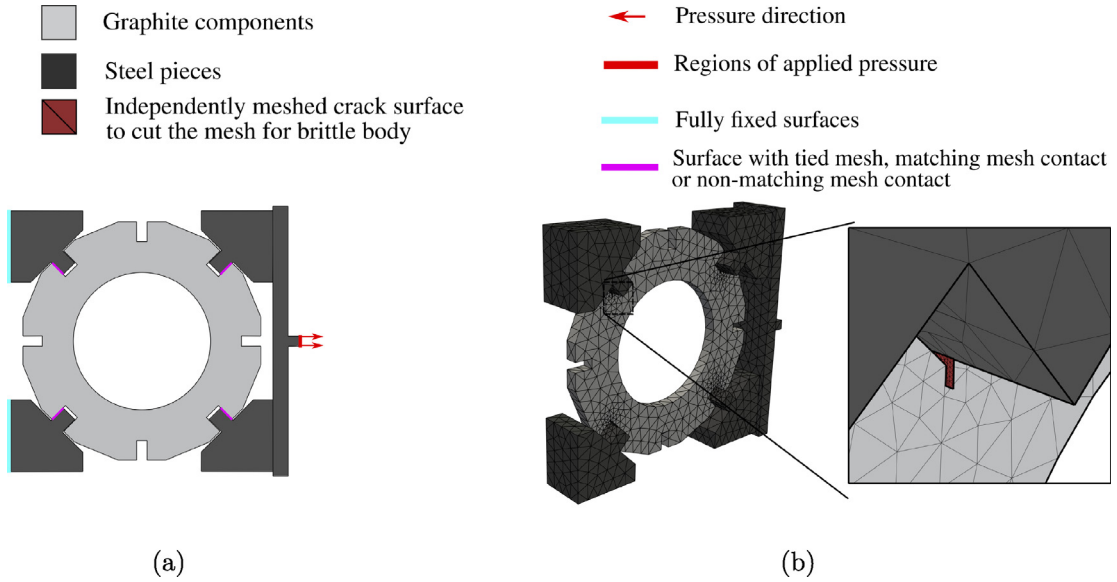
Fig. 15. Brick slice fracture analysis: (a) schematic of the setup and boundary conditions and (b) mesh of the 3D problem and zoom at the location of the initial cutting surface used to seed the crack.
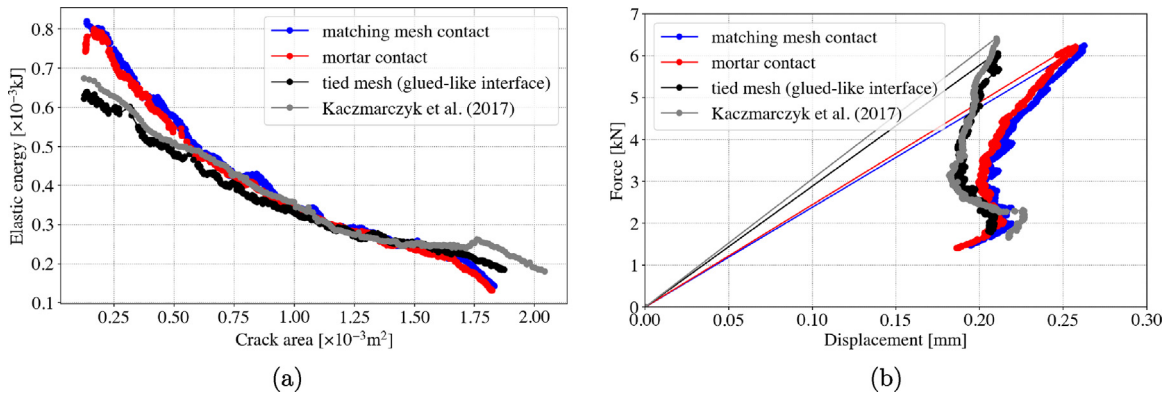

Fig. 16. Comparison of crack propagation for brick slice problem presented in [3] (post-process correction in [103]) between models with tied mesh, matching-meshes contact and non-matching-meshes (mortar) contact.

Table 7
Input parameters brick slice analyses with setup presented in Fig. 15.

g_{cr} [N/mm]	E_{gr} [N/m^2]	ν_{gr}	E_{st} [N/m^2]	ν_{st}	p_g	p_r
0.23	10.9×10^9	0.2	21.0×10^{10}	0.3	2	3

of Kaczmarczyk et al. [3]. Furthermore, all four analyses result to the same curve after the crack surface area reaches 0.5×10^{-3} m^2 indicating that the modelling choice of tied meshes is valid to investigate this particular problem. Furthermore, the dependence of the load on the generalised displacement, defined in [3], is presented in Fig. 16(b) and permits to compare the peak load, for all four cases, which can be associated with the crack initiation load. While matching and non-matching-meshes cases demonstrate similar results, the generalised displacement corresponding to the peak load for the case of tied meshes is different. The reason for such difference is the ability of the tied

Table 8
Input parameters for Case 1 and Case 2 in Fig. 17.

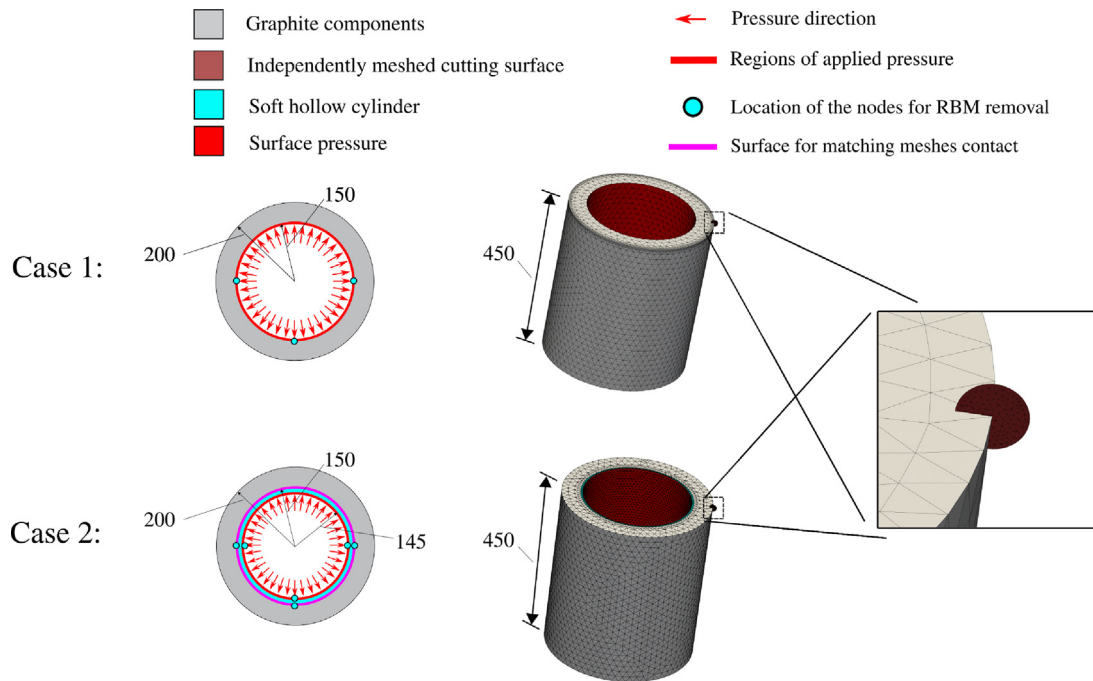| g_{cr} [N/mm]	E_{gr} [N/m^2]	ν_{gr}	E_s [N/m^2]	ν_s	p_g	p_r
0.23	10.9×10^9	0.2	10.9×10^6	0	1	3

Fig. 17. Crack propagation in hollow cylinder where pressure is directly applied to the bore wall in Case 1 or in Case 2 through a thin, soft, hollow, inner cylinder having a conforming contact interface with the outer graphite cylinder.

interface to transfer tangential traction between the bodies, which is absent in frictionless contact, resulting in a stiffer response of the tied mesh. Therefore, contact condition representation is important to better investigate the load–displacement paths of such structures.

5.5. Fracture of hollow cylinder under surface pressure on the bore

Validation of the developed framework for crack propagation along contact interfaces and surfaces under traction is performed using a test which involves fracture of a hollow graphite cylinder. Such cylinder is subjected to uniform surface pressure on the bore, while the initial crack is seeded on the outer surface. Furthermore, Rigid Body Motion is restrained by fixing displacements at 3 points, see Fig. 17. For this validation, two analyses are performed: the first involves only surface pressure boundary conditions and the second one involves surface pressure applied to a hollow soft thin cylinder which has a conforming contact interface with the graphite cylinder with identical material and geometry parameters to that of the first analysis. Details on the geometry of the graphite cylinder and the hollow thin soft cylinder can be found in Fig. 17.

The input parameters for this example are presented in Table 8 where E_{gr}, E_s, ν_{gr} and ν_{gr} are Young's modulus and Poisson's ratio for the graphite and soft cylinder respectively. The material of the inner cylinder in Case 2 was chosen to be soft since it was found that when crack propagates on the contact interface between stiff materials, high strains generated around the crack tip result in gap opening. Therefore, when a non-soft material is used, contact conditions are not active at the crack tip and the first and second case are not fully equivalent. After numerical experimentation, it was found that the thickness of the soft cylinder is not important to acquire the full contact effect.

As the problem is fully symmetric, in both cases the crack propagates vertically along the height of the cylinder. Load versus crack area curve is presented in Fig. 19 and highlighted marks refer to crack surface evolution snapshots
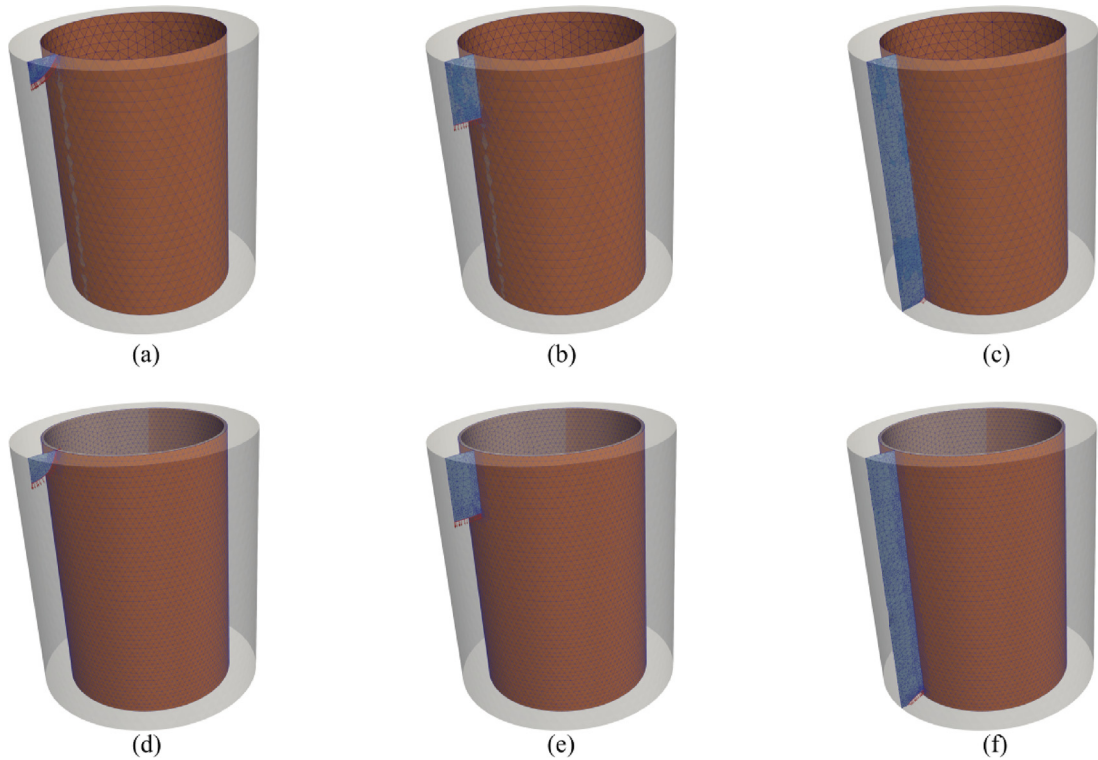
Fig. 18. Crack propagation in a hollow graphite cylinder. In Case 1 - (a), (b), (c) - crack propagates along a surface subjected to normal traction applied at the bore; in Case 2 - (d), (e), (f) - crack front traverses a contact interface between the outer (graphite) and inner (soft) cylinders. Shown snapshots correspond to steps highlighted in Fig. 19.
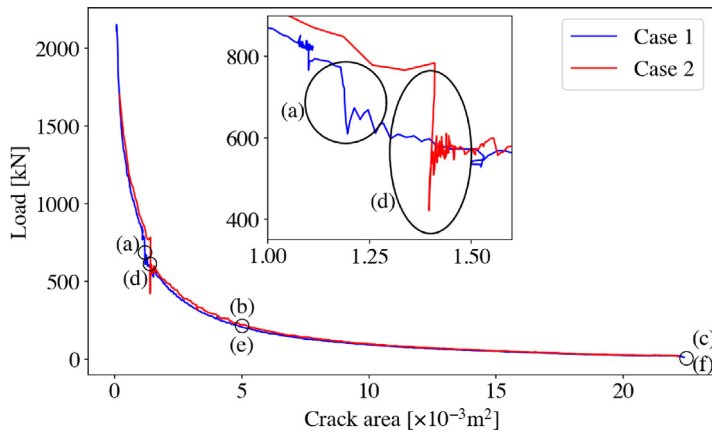

Fig. 19. Dependence of the load on the crack area for hollow graphite cylinder test where marks correspond to crack surface snapshots presented in Fig. 18. The inset shows zoom-in of the plots around points (a) and (d).

shown in Fig. 18. The load is evaluated by multiplying the pressure value by the surface area which slightly differs between the two cases, nevertheless, the results match very well which highlights the robustness of the implementation of the framework.

The vertical jumps of the load marked by (a) and (d) correspond to time steps when crack meets the edge of the inner bore. It is important to note that the present model assumes smooth crack evolution. However, when the crack meets a boundary for the first time (i.e. when percolation occurs), a non-smooth transition takes place and a
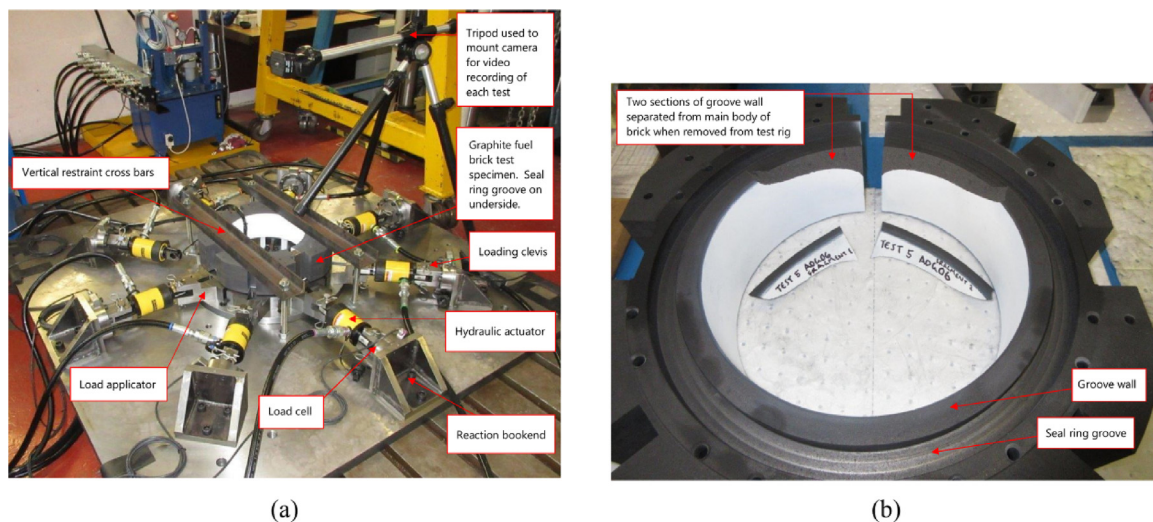
<div align="center">(a)   (b)</div>

Fig. 20. (a) Overview of the test rig for Seal Ring-Groove Wall (SRGW) experiment: brick slice of unirradiated graphite subjected to radial loading via steel collar; (b) Experimental results: failure of the groove wall on the lateral side of the brick slice and separation of two fragments (the brick slice has been turned over for inspection). *Source:* Adopted from [104].

Table 9

Input parameters used for seal ring-groove wall problem.

E_{gr} [MPa]	ν_{gr}	g_{cr} [N/mm]	E_{st} [MPa]	ν_{st}	P [MPa]	p_g	p_r
10.9×10^3	0.2	0.23	210×10^3	0.3	1	1	3

non-differentiable jump of the load is present after which the crack continues to smoothly propagate. The higher the amount of crack front length present on the newly cracked boundary at the time of percolation, the higher the jump observed in the analysis. Furthermore, an oscillation of the curve for the Case 2 (i.e. with the contact interface) is observed due to further mesh topological complexities arising when contact is present. As crack approaches the contact interface, smaller steps are required to resolve complex crack surface morphology until the crack successfully percolates.

5.6. Civil nuclear power generation industry application

The final numerical example involves crack propagation within unirradiated nuclear graphite to simulate an experiment designed and conducted by Hutchinson [104]. The experiment involves fracture of a graphite brick slice (having roughly a hollow cylinder shape) which has a part of its circumference cut and a wedge placed between the two cut surfaces, see Fig. 20(a). The graphite brick slice has a circular groove on the bottom base surface with four ring segments fitted inside. These ring segments are used in practice to seal interfaces between neighbouring bricks stacked in arrays inside the nuclear reactor's core. In the experiment, a steel collar with a groove (similar to that of the brick) is positioned under the brick slice so that the ring segments fit between the two components within their grooves. Radial loading pointing towards the brick centre is applied to the steel collar and transferred to the graphite brick's groove wall through the seal ring segments, causing cracks to start from the inner corners of the groove walls located at the two sides of the wedge. This experiment, called seal ring-groove wall (SRGW) test, results in the generation of two symmetric cracks and detachment of two groove wall fragments of the similar shape presented in Fig. 20(b).

Two analyses were performed to understand the importance of boundary and contact conditions for the crack propagation. In both cases, only half of the problem is analysed taking advantage of the symmetry along axis A–A′ (see Fig. 21). In the first analysis, contact interaction is not taken into account; instead, a uniform pressure is applied on the surfaces where the seal ring segments meet the groove wall. Accordingly, seal ring segments and the loading
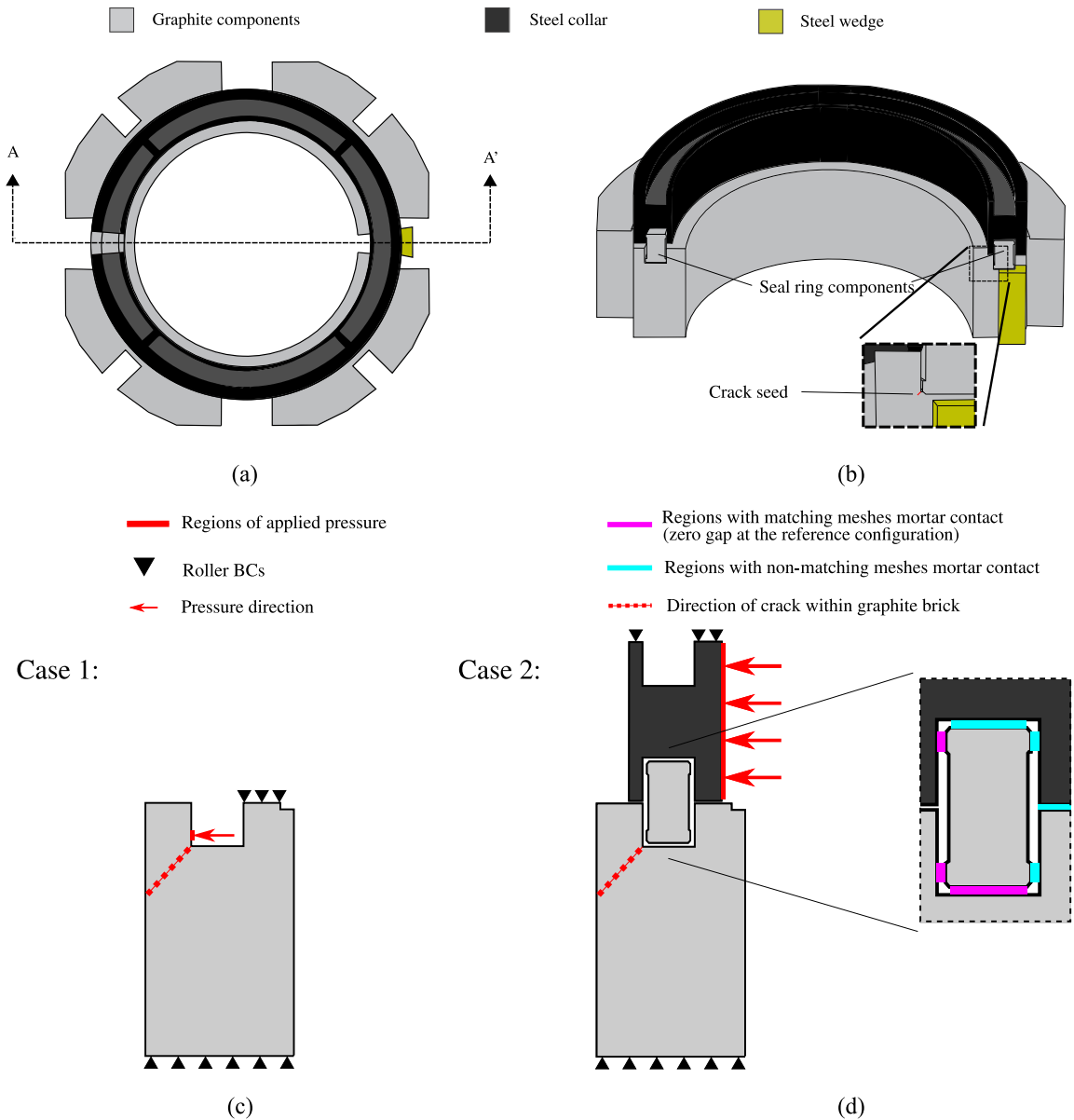
Fig. 21. (a) The experimental setup for crack propagation in graphite brick slice where load applied on the steel collar is transmitted through the seal ring; (b) side view of the A–A' cut of the experimental setup analysed assuming symmetry; (c) steel collar and seal ring components are omitted and pressure is applied directly on the groove wall of the brick (Case 1) and (d) all components and multiple contact interfaces between them are considered and pressure is applied at the exterior part of the steel collar (Case 2).

collar are not present in the Case 1 model. In the second analysis, all components present in the experiment are considered, and the loading is applied on the collar, while multiple contact zones are considered around the seal ring segments as demonstrated in Fig. 21(d), see Table 9 for input parameters.

The load–displacement path for the two setups is presented in Fig. 22. For the case where pressure is applied directly to the groove wall, higher load is needed for the same crack surface increase for the majority of the propagation analysis. This is caused by the increased stiffness of the structure when the steel collar is considered. Note that the drops in Case 2 curve arise from the adjustments of the load factor to allow for crack front rotation due to mesh cutting in challenging configurations. Once the correct crack configuration is found, the load factor
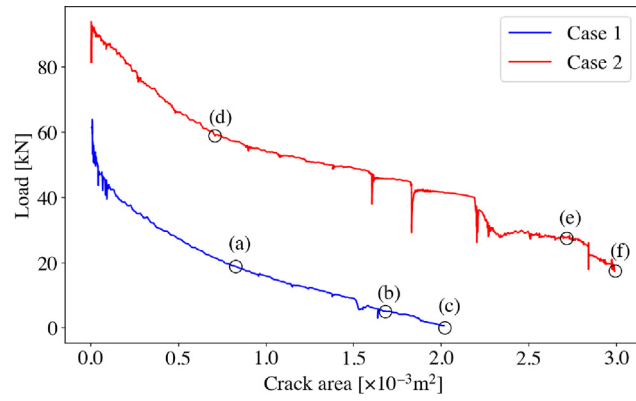
Fig. 22. Load versus crack surface area curves for the SRGW test, Cases 1 and 2. Marks on curves correspond to the crack propagation snapshots presented in Fig. 23.
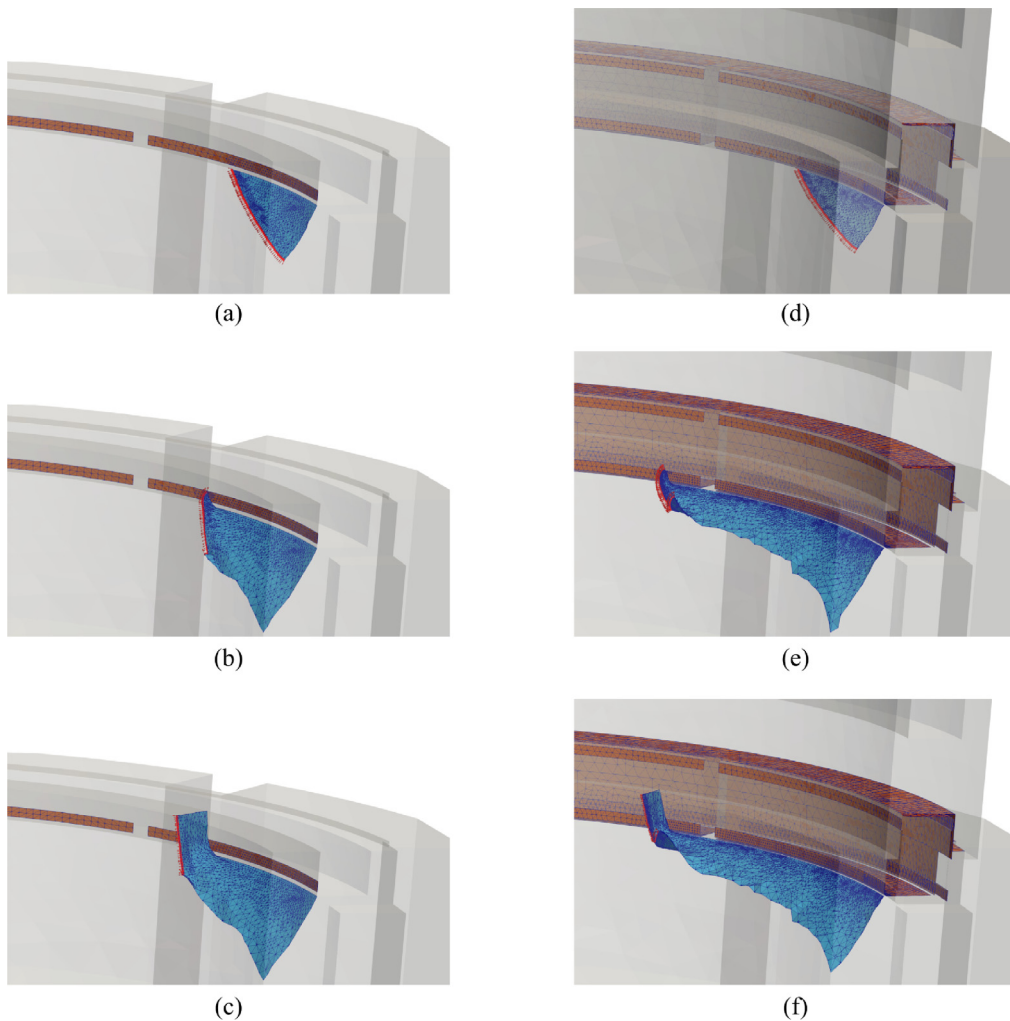

Fig. 23. Crack surface development for points presented in Fig. 22. Case 1: (a), (b), (c); Case 2: (d), (e), (f). Full animated solutions for the crack propagation analysis in both cases can be found in the Supplementary material [94].
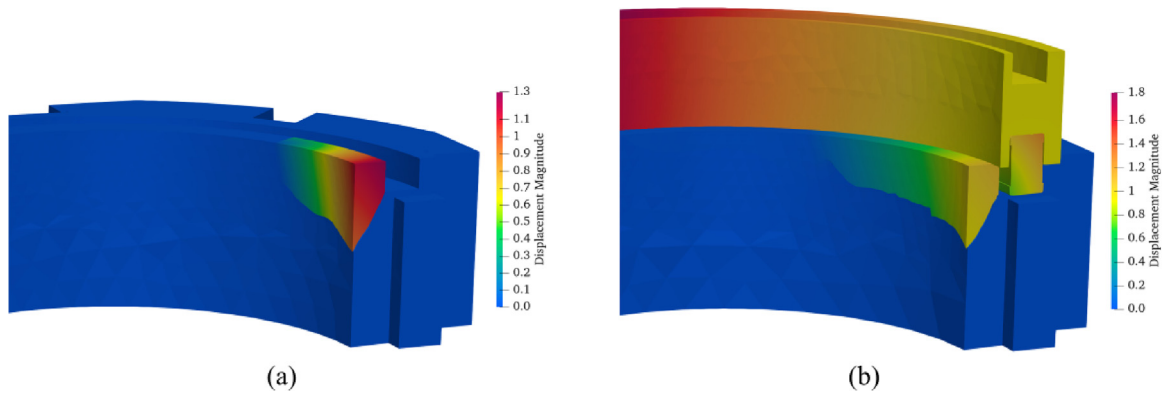
Fig. 24. Deformed shape of last step of seal ring analysis showing detached groove wall fragment for: (a) pressure-induced (Case 1) and (b) contact-induced crack propagation (Case 2). Colourmaps represent the displacement magnitude in mm.
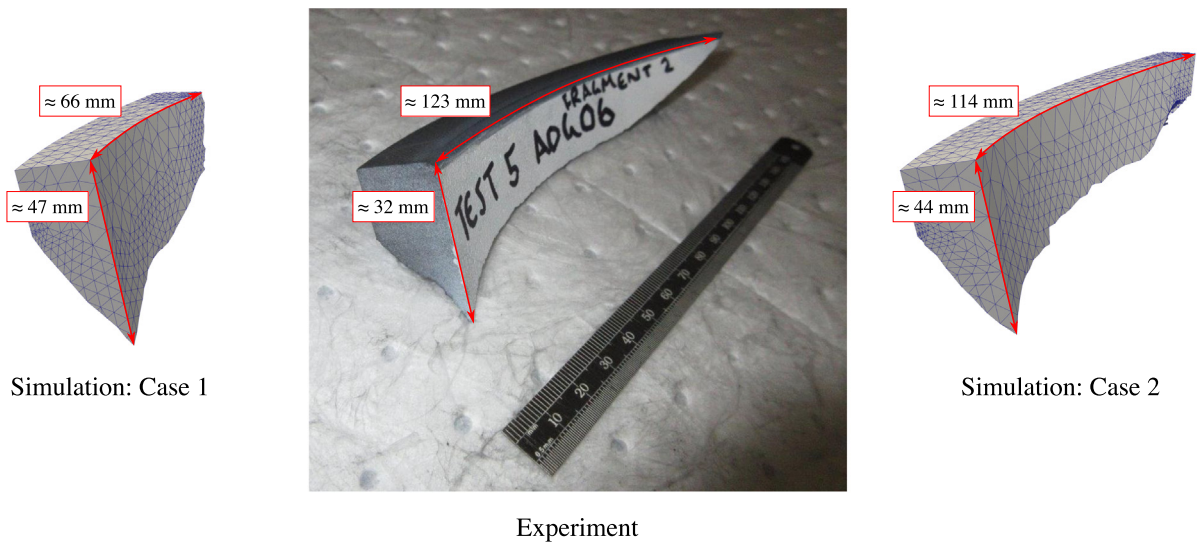

Fig. 25. Geometry of the fragment detached from the groove wall in the experiment [104] and simulation for both cases 1 and 2 (note that the geometry obtained in simulation was mirrored for visual comparison with one of the two almost identical fragments detached from two sides of the brick in the experiment).

returns to approximately the same value as it was before such drop. Furthermore, in Fig. 23, three snapshots of crack surface are shown for each of the models corresponding to marks in Fig. 22. Note that during crack propagation in Case 1, the crack traverses the pressure zone on the groove wall, see Fig. 23(b), while in Case 2, the crack propagates along the contact interface between the groove wall and the seal ring, see Fig. 23(d). The developed framework enables robust analysis for both cases.

The deformed shape of the setup corresponding to the last step of the SRGW fracture analyses is presented in Fig. 24 for both Cases 1 and 2. Furthermore, the geometry of the fragment detached from the groove wall observed in the experiment is compared in Fig. 25 with the results of simulation. In both cases, the overall fragment geometry is similar to the experimental one, however, the fragment produced in Case 2 simulation has dimensions closer to the experimental observation. Therefore, it is evident that for the this problem, consideration of all components and multiple contact interfaces (as was done in Case 2 analysis) is essential to bring the simulation results closer to the experimental observations.

6. Conclusions

In this paper we proposed an implicit and thermodynamically consistent formulation for simulating brittle fracture along contact interfaces and surfaces under load. The problem involves two coupled unilateral constraints: for crack propagation and for contact interaction. All governing equations and constraints are solved monolithically using the Newton–Raphson method.

The discretisation of equations resulting from the interaction between the crack and surfaces under load were discussed. The contribution of the surface traction to the configurational forces was shown to be crucial for the correct computation of the crack energy release rate and, consequently, for the correct simulation of the evolution of the crack surface. Furthermore, a novel approach for handling the distortion of the contact elements in the neighbourhood of the crack front was shown to be effective for modelling the interaction of the crack and the contact.

The implementation was verified via several examples, including comparison with existing analytical solutions, published computational and experimental results. The robustness of the implementation was demonstrated on several challenging examples, including crack propagation along contact interfaces and surfaces under pressure.

The framework was used to simulate an industrial problem involving brittle fracture of graphite components similar to those found in Advanced Gas-cooled Reactors. Two cases were considered: one neglecting contact interaction and the second one considering multiple contact zones. In the first case, the crack traversed a pressure surface; in the second case, the crack propagated along a contact interface. The results obtained, including the shapes of the detached graphite fragments, compared favourably to those observed in experiments. However, the second model, which included contact interactions, better approximated the physical reality.

This framework can be used to solve a class of problems involving fracture, where the crack is propagating along contact interfaces between components. The generality of the presented framework enables the further extension to dynamic cases of crack propagation and ductile fracture. In the future, the model will be extended to consider frictional contact, large strains and large displacements. Moreover, Lagrange multipliers enforcing contact constraints will be approximated using a variationally consistent functional space. Furthermore, concepts proposed in this paper related to ALE formulation can be used for a broader class of problems, such as Fluid–Structure Interaction, rolling contact and wear.

The proposed numerical scheme offers a unique combination of the thermodynamically consistent simulation of crack surface evolution, fully coupled with crack propagation along the contact interfaces and surfaces under traction, an implicit formulation and error control provided by hp-adaptivity.

Declaration of competing interest

The authors declare the following financial interests/personal relationships which may be considered as potential competing interests: Chris Pearce and Łukasz Kaczmarczyk reports financial support was provided by EDF Energy Nuclear Generation Ltd. Chris Pearce reports financial support was provided by The Royal Academy of Engineering.

Data availability

The code associated with this publication is open-source. Data used in the paper, such as meshes and parameter files, are available to download via the DOI link on Zenodo. DOI for data is referenced in the paper.

Acknowledgements

Appendix A. Surface traction element in the ALE description

The linearisation of the surface traction element for ALE formulation reads:

$$
\begin{bmatrix}
\mathbf{0} & \dfrac{\partial \mathscr{T}_i^{\mathrm{sp},s_{\mathrm{r}}}}{\partial \tilde{X}_I^{m_{\mathrm{c}}}} \\[2ex]
\dfrac{\partial \mathscr{T}_I^{\mathrm{mat},m_{\mathrm{r}}}}{\partial \tilde{x}_i^{s_{\mathrm{c}}}} & \dfrac{\partial \mathscr{T}_I^{\mathrm{mat},m_{\mathrm{r}}}}{\partial \tilde{X}_I^{m_{\mathrm{c}}}}
\end{bmatrix}
\begin{bmatrix}
\Delta \tilde{x}_i^{s_{\mathrm{r}}} \\[1ex]
\Delta \tilde{X}_I^{m_{\mathrm{r}}}
\end{bmatrix}
= -
\begin{bmatrix}
\mathscr{T}_i^{\mathrm{sp},s_{\mathrm{r}}} \\[1ex]
\mathscr{T}_I^{\mathrm{mat},m_{\mathrm{r}}}
\end{bmatrix}
\tag{A.1}
$$

where superscripts m_{r}, m_{c}, s_{r} and s_{c} refer to materials rows, material columns, spatial rows and spatial columns indices, respectively. The LHS term, $\dfrac{\partial \mathscr{T}_i^{\mathrm{sp},s_{\mathrm{r}}}}{\partial \tilde{X}_I^{m_{\mathrm{c}}}}$, is non-zero only for the elements located at the trace of the smoothing bubble on the surface of the body, $\Gamma_{\sigma,\mathrm{sb}}^{\mathrm{h}}$. It is important to clarify that the derivative with respect to degrees of freedom $\dfrac{\partial \mathscr{T}_i^{\mathrm{sp},s_{\mathrm{r}}}}{\partial \tilde{X}_I^{m_{\mathrm{c}}}}$ does not imply that surface pressure offers any work input to the material nodes. The emergence of this LHS term is due to the movement of material nodes caused by mesh smoothing which in turn generates variation of $\hat{N}_J^{\mathrm{h}}$ that must be accounted for.

Appendix B. Linearisation of transpose of deformation gradient tensor

The linearisation of the transpose of the deformation gradient tensor, F_{Ji}^{h}, in (49) is given by

$$
\frac{\partial F_{iJ}^{\mathrm{h}}}{\partial \tilde{X}_K^m} = h_{i\alpha}^{\mathrm{h}} \frac{\partial \left(H_{J\alpha}^{\mathrm{h}}\right)^{-1}}{\partial \tilde{X}_K^m} \quad \text{with} \quad \frac{\partial \left(H_{J\alpha}^{\mathrm{h}}\right)^{-1}}{\partial \tilde{X}_K^m} = -\left(H_{J\alpha}^{\mathrm{h}}\right)^{-1} \frac{\partial M^m}{\partial \chi_\beta} \left(H_{K\beta}^{\mathrm{h}}\right)^{-1},
\tag{B.1}
$$

as described in Chapter 4 in [105].

Appendix C. Mortar contact element in the ALE description

The linearisation of the contact element for ALE formulation reads:

$$
\begin{bmatrix}
\mathbf{0} & \mathbf{0} & \dfrac{\partial \mathscr{Q}_i^{(1),s_{\mathrm{r}}}}{\partial \tilde{X}_I^{(1),m_{\mathrm{c}}}} & \mathbf{0} & \dfrac{\partial \mathscr{Q}_i^{(1),s_{\mathrm{r}}}}{\partial \tilde{\lambda}^{c_{\mathrm{c}}}} \\[2ex]
\mathbf{0} & \mathbf{0} & \dfrac{\partial \mathscr{Q}_i^{(2),s_{\mathrm{r}}}}{\partial \tilde{X}_I^{(1),m_{\mathrm{c}}}} & \dfrac{\partial \mathscr{Q}_i^{(2),s_{\mathrm{r}}}}{\partial \tilde{X}_I^{(2),m_{\mathrm{c}}}} & \dfrac{\partial \mathscr{Q}_i^{(2),s_{\mathrm{r}}}}{\partial \tilde{\lambda}^{c_{\mathrm{c}}}} \\[2ex]
\dfrac{\partial \mathscr{R}_I^{(1),m_{\mathrm{r}}}}{\partial \tilde{x}_i^{(1),s_{\mathrm{c}}}} & \mathbf{0} & \dfrac{\partial \mathscr{R}_I^{(1),m_{\mathrm{r}}}}{\partial \tilde{X}_I^{(1),m_{\mathrm{c}}}} & \mathbf{0} & \dfrac{\partial \mathscr{R}_I^{(1),m_{\mathrm{r}}}}{\partial \tilde{\lambda}^{c_{\mathrm{c}}}} \\[2ex]
\mathbf{0} & \dfrac{\partial \mathscr{R}_I^{(2),m_{\mathrm{r}}}}{\partial \tilde{x}_i^{(2),s_{\mathrm{c}}}} & \dfrac{\partial \mathscr{R}_I^{(2),m_{\mathrm{r}}}}{\partial \tilde{X}_I^{(1),m_{\mathrm{c}}}} & \dfrac{\partial \mathscr{R}_I^{(2),m_{\mathrm{r}}}}{\partial \tilde{X}_I^{(2),m_{\mathrm{c}}}} & \dfrac{\partial \mathscr{R}_I^{(2),m_{\mathrm{r}}}}{\partial \tilde{\lambda}^{c_{\mathrm{c}}}} \\[2ex]
\dfrac{\partial \mathscr{C}_{\mathrm{con}}^{c_{\mathrm{r}}}}{\partial \tilde{x}_i^{(1),s_{\mathrm{c}}}} & \dfrac{\partial \mathscr{C}_{\mathrm{con}}^{c_{\mathrm{r}}}}{\partial \tilde{x}_i^{(2),s_{\mathrm{c}}}} & \dfrac{\partial \mathscr{C}_{\mathrm{con}}^{c_{\mathrm{r}}}}{\partial \tilde{X}_I^{(1),m_{\mathrm{c}}}} & \mathbf{0} & \dfrac{\partial \mathscr{C}_{\mathrm{con}}^{c_{\mathrm{r}}}}{\partial \tilde{\lambda}^{c_{\mathrm{c}}}}
\end{bmatrix}
\begin{bmatrix}
\Delta \tilde{x}_i^{(1),s_{\mathrm{r}}} \\[1ex]
\Delta \tilde{x}_i^{(2),s_{\mathrm{r}}} \\[1ex]
\Delta \tilde{X}_I^{(1),m_{\mathrm{r}}} \\[1ex]
\Delta \tilde{X}_I^{(2),m_{\mathrm{r}}} \\[1ex]
\Delta \tilde{\lambda}_i^{s_{\mathrm{r}}}
\end{bmatrix}
= -
\begin{bmatrix}
\mathscr{Q}_i^{(1),s_{\mathrm{r}}} \\[1ex]
\mathscr{Q}_i^{(2),s_{\mathrm{r}}} \\[1ex]
\mathscr{R}_I^{(1),m_{\mathrm{r}}} \\[1ex]
\mathscr{R}_I^{(2),m_{\mathrm{r}}} \\[1ex]
\mathscr{C}_{\mathrm{con}}^{c_{\mathrm{r}}}
\end{bmatrix}
\tag{C.1}
$$

Rows corresponding to either $\mathscr{R}_I^{(1),m_{\mathrm{r}}}$ or $\mathscr{R}_I^{(2),m_{\mathrm{r}}}$ are zero depending on whether the crack crosses the master or the slave surface, respectively. Furthermore, rows related to $\mathscr{R}_I^{(2),m_{\mathrm{r}}}$ and $\mathscr{Q}_i^{(2),s_{\mathrm{r}}}$ have derivatives in the tangent matrix for both $\tilde{X}_I^{(1),m_{\mathrm{r}}}$ and $\tilde{X}_I^{(2),m_{\mathrm{r}}}$ as the unit normal $\hat{N}_J^{\mathrm{h}}$ is defined on the slave side and integration is performed on the material side and therefore the determinant of the Jacobian is differentiable with respect to the master side degrees of freedom.

References

[1] C. Miehe, H. Dal, L.-M. Schänzel, A. Raina, A phase-field model for chemo-mechanical induced fracture in lithium-ion battery electrode particles, Internat. J. Numer. Methods Engrg. 106 (2016) 683–711.

[2] Ł. Kaczmarczyk, M.M. Nezhad, C. Pearce, Three-dimensional brittle fracture: configurational-force-driven crack propagation, Internat. J. Numer. Methods Engrg. 97 (2014) 531–550.

[3] Ł. Kaczmarczyk, Z. Ullah, C.J. Pearce, Energy consistent framework for continuously evolving 3d crack propagation, Comput. Methods Appl. Mech. Engrg. 324 (2017) 54–73.

[4] T. Rabczuk, Computational methods for fracture in brittle and quasi-brittle solids: state-of-the-art review and future perspectives, Int. Sch. Res. Notices 2013 (2013).

[5] J.-H. Song, T. Belytschko, Cracking node method for dynamic fracture with finite elements, Internat. J. Numer. Methods Engrg. 77 (2009) 360–385.

[6] T. Strouboulis, K. Copps, I. Babuša, The generalized finite element method: an example of its implementation and illustration of its performance, Internat. J. Numer. Methods Engrg. 47 (2000) 1401–1417.

[7] N. Moës, J. Dolbow, T. Belytschko, A finite element method for crack growth without remeshing, Internat. J. Numer. Methods Engrg. 46 (1999) 131–150.

[8] T. Belytschko, T. Black, Elastic crack growth in finite elements with minimal remeshing, Internat. J. Numer. Methods Engrg. 45 (1999) 601–620.

[9] I. Babuša, J.M. Melenk, The partition of unity method, Internat. J. Numer. Methods Engrg. 40 (1997) 727–758.

[10] J. Mosler, G. Meschke, 3D modelling of strong discontinuities in elastoplastic solids: fixed and rotating localization formulations, Internat. J. Numer. Methods Engrg. 57 (2003) 1553–1576.

[11] D.C. Thompson, P.P. Pebay, Embarrassingly parallel mesh refinement by edge subdivision, Eng. Comput. 22 (2006) 75–93.

[12] G.N. Wells, L. Sluys, A new method for modelling cohesive cracks using finite elements, Internat. J. Numer. Methods Engrg. 50 (2001) 2667–2682.

[13] Z.P. Bažnt, B.H. Oh, Crack band theory for fracture of concrete, Matér. Constr. 16 (1983) 155–177.

[14] P. Grassl, M. Jirásek, Damage-plastic model for concrete failure, Int. J. Solids Struct. 43 (2006) 7166–7196.

[15] C. Miehe, F. Welschinger, M. Hofacker, Thermodynamically consistent phase-field models of fracture: Variational principles and multi-field fe implementations, Internat. J. Numer. Methods Engrg. 83 (2010) 1273–1311.

[16] R.H. Peerlings, R. de Borst, W.M. Brekelmans, J. de Vree, Gradient enhanced damage for quasi-brittle materials, Internat. J. Numer. Methods Engrg. 39 (1996) 3391–3403.

[17] R. de Borst, J. Pamin, M.G. Geers, On coupled gradient-dependent plasticity and damage theories with a view to localization analysis, Eur. J. Mech. A Solids 18 (1999) 939–962.

[18] R. de Borst, C.V. Verhoosel, Gradient damage vs phase-field approaches for fracture: Similarities and differences, Comput. Methods Appl. Mech. Engrg. 312 (2016) 78–94.

[19] N.M. Azevedo, J. Lemos, Hybrid discrete element/finite element method for fracture analysis, Comput. Methods Appl. Mech. Engrg. 195 (2006) 4579–4593.

[20] J. Kozicki, F.V. Donze, A new open-source software developed for numerical simulations using discrete modeling methods, Comput. Methods Appl. Mech. Engrg. 197 (2008) 4429–4443.

[21] P. Grassl, M. Jirásek, Meso-scale approach to modelling the fracture process zone of concrete subjected to uniaxial tension, Int. J. Solids Struct. 47 (2010) 957–968.

[22] J. Bolander Jr., S. Saito, Fracture analyses using spring networks with random geometry, Eng. Fract. Mech. 61 (1998) 569–591.

[23] Y.D. Ha, F. Bobaru, Characteristics of dynamic brittle fracture captured with peridynamics, Eng. Fract. Mech. 78 (2011) 1156–1168.

[24] J.D. Eshelby, The force on an elastic singularity, Philos. Trans. R. Soc. Lond. Ser. A Math. Phys. Sci. 244 (1951) 87–112.

[25] J.D. Eshelby, Energy relations and the energy–momentum tensor in continuum mechanics, in: The Energy Momentum Tensor in Continuum Mechanics, Inelastic Behavior of Solids, 1970, pp. 77–115.

[26] G.A. Maugin, C. Trimarco, Pseudomomentum and material forces in nonlinear elasticity: variational formulations and application to brittle fracture, Acta Mech. 94 (1992) 1–28.

[27] M.E. Gurtin, P. Podio-Guidugli, Configurational forces and the basic laws for crack propagation, J. Mech. Phys. Solids 44 (1996) 905–927.

[28] P. Steinmann, D. Ackermann, F. Barth, Application of material forces to hyperelastostatic fracture mechanics. II. computational setting, Int. J. Solids Struct. 38 (2001) 5509–5526.

[29] C. Miehe, E. Güses, M. Birkle, A computational framework of configurational-force-driven brittle fracture based on incremental energy minimization, Int. J. Fract. 145 (2007) 245–259.

[30] E. Güses, C. Miehe, A computational framework of three-dimensional configurational-force-driven brittle crack propagation, Comput. Methods Appl. Mech. Engrg. 198 (2009) 1413–1428.

[31] R. Bird, W. Coombs, S. Giani, A quasi-static discontinuous galerkin configurational force crack propagation method for brittle materials: discontinuous Galerkin configurational force crack propagation, Internat. J. Numer. Methods Engrg. 113 (2018) 1061–1080.

[32] R. Bird, W.M. Coombs, S. Giani, Adaptive configurational force-based propagation for brittle and fatigue crack analysis, Internat. J. Numer. Methods Engrg. 123 (2022) 1673–1709.

[33] I. Khisamitov, G. Meschke, Configurational-force interface model for brittle fracture propagation, Comput. Methods Appl. Mech. Engrg. 351 (2019) 351–378.

[34] A. Farrokhnia, A.P. Jivkov, G. Hall, P. Mummery, Large-scale modeling of damage and failure of nuclear graphite moderated reactor, J. Press. Vessel Technol. 144 (2022).

[35] V.A. Yastrebov, Numerical Methods in Contact Mechanics, John Wiley & Sons, 2013.

[36] P. Alart, A. Curnier, A mixed formulation for frictional contact problems prone to Newton like solution methods, Comput. Methods Appl. Mech. Engrg. 92 (1991) 353–375.

[37] S. Hüber, B. Wohlmuth, A primal–dual active set strategy for non-linear multibody contact problems, Comput. Methods Appl. Mech. Engrg. 194 (2005) 3147–3166.

[38] M. Puso, T. Laursen, A mortar segment-to-segment contact method for large deformation solid mechanics, Comput. Methods Appl. Mech. Engrg. 193 (2004) 601–629.

[39] A. Popp, M. Gitterle, M. Gee, W. Wall, A dual mortar approach for 3d finite deformation contact with consistent linearization, Internat. J. Numer. Methods Engrg. 83 (2010) 1428–1465.

[40] M. Poluektov, L. Figiel, A cut finite-element method for fracture and contact problems in large-deformation solid mechanics, Comput. Methods Appl. Mech. Engrg. 388 (2022) 114234.

[41] I. Stefansson, I. Berre, E. Keilegavlen, A fully coupled numerical model of thermo-hydro-mechanical processes and fracture contact mechanics in porous media, Comput. Methods Appl. Mech. Engrg. 386 (2021) 114122.

[42] M. Nejati, A. Paluszny, R.W. Zimmerman, A finite element framework for modeling internal frictional contact in three-dimensional fractured media using unstructured tetrahedral meshes, Comput. Methods Appl. Mech. Engrg. 306 (2016) 123–150.

[43] H. Fang, D. Zhang, M. Zhou, Q. Fang, M. Wen, A contact algorithm for cohesive cracks in the extended finite element method, Internat. J. Numer. Methods Engrg. 121 (2020) 2747–2766.

[44] A.R. Khoei, B. Bahmani, Application of an enriched FEM technique in thermo-mechanical contact problems, Comput. Mech. 62 (2018) 1127–1154.

[45] L. Rodríguez-Tembleque, F. García-Sánchez, A. Sáez, Crack-face frictional contact modelling in cracked piezoelectric materials, Comput. Mech. 64 (2019) 1655–1667.

[46] M.R. Hirmand, M. Vahab, K.D. Papoulia, N. Khalili, Energy minimization versus criteria-based methods in discrete cohesive fracture simulations, Comput. Mech. 68 (2021) 845–860.

[47] F. Fei, J. Choo, A phase-field method for modeling cracks with frictional contact, Internat. J. Numer. Methods Engrg. 121 (2020) 740–762.

[48] P. Zhang, C. Du, W. Zhao, L. Sun, Dynamic crack face contact and propagation simulation based on the scaled boundary finite element method, Comput. Methods Appl. Mech. Engrg. 385 (2021) 114044.

[49] M. Pundir, G. Anciaux, Coupling between cohesive element method and node-to-segment contact algorithm: Implementation and application, Internat. J. Numer. Methods Engrg. 122 (2021) 4333–4353.

[50] H. Cheng, X. Zhou, New technique for frictional contact on crack slip in the extended finite-element method framework, J. Eng. Mech. 144 (2018) 04018059.

[51] F. Liu, R.I. Borja, A contact algorithm for frictional crack propagation with the extended finite element method, Internat. J. Numer. Methods Engrg. 76 (2008) 1489–1512.

[52] J. Dolbow, N. Moë, T. Belytschko, An extended finite element method for modeling crack growth with frictional contact, Comput. Methods Appl. Mech. Engrg. 190 (2001) 6825–6846.

[53] H. Cheng, X. Zhou, Numerical simulation of the dynamic frictional contact problem for crack slip based on the multidimensional space method, J. Eng. Mech. 145 (2019) 04018128.

[54] H. Dang-Trung, E. Keilegavlen, I. Berre, Numerical modeling of wing crack propagation accounting for fracture contact mechanics, Int. J. Solids Struct. 204–205 (2020) 233–247.

[55] E. Giner, M. Tur, J.E. Tarancón, F.J. Fuenmayor, Crack face contact in x-fem using a segment-to-segment approach, Internat. J. Numer. Methods Engrg. 82 (2010) 1424–1449.

[56] E. Giner, M. Tur, A. Vercher, F. Fuenmayor, Numerical modelling of crack–contact interaction in 2d incomplete fretting contacts using x-fem, Tribol. Int. 42 (2009) 1269–1275.

[57] F. Meray, T. Chaise, A. Gravouil, P. Depouhon, B. Descharrieres, D. Nélias, A novel sam/x-fem coupling approach for the simulation of 3d fatigue crack growth under rolling contact loading, Finite Elem. Anal. Des. 206 (2022) 103752.

[58] T. Hu, J. Guilleminot, J.E. Dolbow, A phase-field model of fracture with frictionless contact and random fracture properties: Application to thin-film fracture and soil desiccation, Comput. Methods Appl. Mech. Engrg. 368 (2020) 113106.

[59] A. de Pannemaecker, S. Fouvry, J. Buffiere, M. Brochu, Modelling the fretting fatigue crack growth: From short crack correction strategies to microstructural approaches, Int. J. Fatigue 117 (2018) 75–89.

[60] S. Mai, A. Gravouil, M. Nguyen-Tajan, B. Trollé, Numerical simulation of rolling contact fatigue crack growth in rails with the rail bending and the frictional contact, Eng. Fract. Mech. 174 (2017) 196–206.

[61] R. Ribeaucourt, M.-C. Baietto-Dubourg, A. Gravouil, A new fatigue frictional contact crack propagation model with the coupled x-fem/latin method, Comput. Methods Appl. Mech. Engrg. 196 (2007) 3230–3247.

[62] W. Daves, M. Kráčík, S. Scheriau, Analysis of crack growth under rolling-sliding contact, Int. J. Fatigue 121 (2019) 63–72.

[63] M. Farjoo, W. Daniel, P.A. Meehan, Modelling a squat form crack on a rail laid on an elastic foundation, Eng. Fract. Mech. 85 (2012) 47–58.

[64] B. Carter, E. Schenck, P. Wawrzynek, A. Ingraffea, K. Barlow, Three-dimensional simulation of fretting crack nucleation and growth, Eng. Fract. Mech. 96 (2012) 447–460.

[65] Z. Anjum, F. Qayyum, S. Khushnood, S. Ahmed, M. Shah, Prediction of non-propagating fretting fatigue cracks in ti6al4v sheet tested under pin-in-dovetail configuration: Experimentation and numerical simulation, Mater. Des. 87 (2015) 750–758.

[66] C. Hu, D. Wei, Y. Wang, L. Shi, Experimental and numerical study of fretting fatigue in dovetail assembly using a total life prediction model, Eng. Fract. Mech. 205 (2019) 301–318.

[67] M.A. Homel, E.B. Herbold, Field-gradient partitioning for fracture and frictional contact in the material point method, Internat. J. Numer. Methods Engrg. 109 (2017) 1013–1044.

[68] E.G. Kakouris, S.P. Triantafyllou, Phase-field material point method for dynamic brittle fracture with isotropic and anisotropic surface energy, Comput. Methods Appl. Mech. Engrg. 357 (2019).

[69] C. Hesch, M. Franke, M. Dittmann, I. Tamizer, Hierarchical nurbs and a higher-order phase-field approach to fracture for finite-deformation contact problems, Comput. Methods Appl. Mech. Engrg. 301 (2016) 242–258.

[70] M. Krü, M. Dittmann, F. Aldakheel, A. Hä, P. Wriggers, C. Hesch, Porous-ductile fracture in thermo-elasto-plastic solids with contact applications, Comput. Mech. 65 (2020) 941–966.

[71] M. Dittmann, M. Krü, F. Schmidt, S. Schuß, C. Hesch, Variational modeling of thermomechanical fracture and anisotropic frictional mortar contact problems with adhesion, Comput. Mech. 63 (2019) 571–591.

[72] K. Lewandowski, L. Kaczmarczyk, I. Athanasiadis, J.F. Marshall, C.J. Pearce, A computational framework for crack propagation in spatially heterogeneous materials, Phil. Trans. R. Soc. A 379 (2021) 20200291.

[73] J.E. Marsden, T.J.R. Hughes, Mathematical Foundations of Elasticity, Dover, 1994.

[74] G.A. Holzapfel, Nonlinear Solid Mechanics: A Continuum Approach for Engineering, Wiley, 2000.

[75] M. Lazar, H.O. Kirchner, The eshelby stress tensor, angular momentum tensor and dilatation flux in gradient elasticity, Int. J. Solids Struct. 44 (2007) 2477–2486.

[76] M. Brü, Eshelby stress tensor in large strain anisotropic damage mechanics, Int. J. Mech. Sci. 46 (2004) 1763–1782.

[77] J.R. Rice, A path independent integral and the approximate analysis of strain concentration by notches and cracks, J. Appl. Mech. 35 (1968) 379–386.

[78] A. Popp, M. Gee, W. Wall, A finite deformation mortar contact formulation using a primal–dual active set strategy, Internat. J. Numer. Methods Engrg. 79 (2009) 1354–1391.

[79] J. Heegaard, A. Curnier, An augmented lagrangian method for discrete large-slip contact problems, Internat. J. Numer. Methods Engrg. 36 (1993) 569–593.

[80] M. Ainsworth, J. Coyle, Hierarchic finite element bases on unstructured tetrahedral meshes, Internat. J. Numer. Methods Engrg. 58 (2003) 2103–2130.

[81] M. Joshaghani, S. Joodat, K. Nakshatrala, A stabilized mixed discontinuous Galerkin formulation for double porosity/permeability model, Comput. Methods Appl. Mech. Engrg. 352 (2019) 508–560.

[82] R. Sevilla, M. Giacomini, A. Karkoulias, A. Huerta, A superconvergent hybridisable discontinuous galerkin method for linear elasticity: A superconvergent hybridisable discontinuous Galerkin method for linear elasticity, Internat. J. Numer. Methods Engrg. 116 (2018) 91–116.

[83] V.M. Calo, A. Ern, I. Muga, S. Rojas, An adaptive stabilized conforming finite element method via residual minimization on dual discontinuous Galerkin norms, Comput. Methods Appl. Mech. Engrg. 363 (2020) 112891.

[84] J. Muñoz-Matute, D. Pardo, L. Demkowicz, A DPG-based time-marching scheme for linear hyperbolic problems, Comput. Methods Appl. Mech. Engrg. 373 (2021) 113539.

[85] A. Vaziri Astaneh, F. Fuentes, J. Mora, L. Demkowicz, High-order polygonal discontinuous Petrov–Galerkin (PolyDPG) methods using ultraweak formulations, Comput. Methods Appl. Mech. Engrg. 332 (2018) 686–711.

[86] P. Wriggers, G. Zavarise, A formulation for frictionless contact problems using a weak form introduced by Nitsche, Comput. Mech. 41 (2008) 407–420.

[87] A. Seitz, W.A. Wall, A. Popp, Nitsche's method for finite deformation thermomechanical contact problems, Comput. Mech. 63 (2019) 1091–1110.

[88] M. Hiermeier, W.A. Wall, A. Popp, A truly variationally consistent and symmetric mortar-based contact formulation for finite deformation solid mechanics, Comput. Methods Appl. Mech. Engrg. 342 (2018) 532–560.

[89] A. Popp, A. Seitz, M. Gee, W. Wall, Improved robustness and consistency of 3d contact algorithms based on a dual mortar approach, Comput. Methods Appl. Mech. Engrg. 264 (2013) 67–80.

[90] P. Farah, A. Popp, W. Wall, Segment-based vs. element-based integration for mortar methods in computational contact mechanics, Comput. Mech. 55 (2015) 209–228.

[91] Ł. Kaczmarczyk, Z. Ullah, K. Lewandowski, X. Meng, X.-Y. Zhou, I. Athanasiadis, H. Nguyen, C.-A. Chalons-Mouriesse, E. Richardson, E. Miur, A. Shvarts, M. Wakeni, C. Pearce, MoFEM: an open source, parallel finite element library, J. Open Source Softw. (2020) http://dx.doi.org/10.21105/joss.01441, URL: https://joss.theoj.org/papers/10.21105/joss.01441, http://mofem.eng.gla.ac.uk.

[92] S. Balay, S. Abhyankar, M.F. Adams, S. Benson, J. Brown, P. Brune, K. Buschelman, E.M. Constantinescu, L. Dalcin, A. Dener, V. Eijkhout, W.D. Gropp, V. Hapla, T. Isaac, P. Jolivet, D. Karpeev, D. Kaushik, M.G. Knepley, F. Kong, S. Kruger, D.A. May, L.C. McInnes, R.T. Mills, L. Mitchell, T. Munson, J.E. Roman, K. Rupp, P. Sanan, J. Sarich, B.F. Smith, S. Zampini, H. Zhang, H. Zhang, J. Zhang, PETSc web page, 2022, URL: https://petsc.org/.

[93] T.J. Tautges, C. Ernst, C. Stimpson, R.J. Meyers, K. Merkley, Moab : a mesh-oriented database, 2004.

[94] I. Athanasiadis, A.G. Shvarts, L. Kaczmarczyk, Z. Ullah, K. Lewandowski, C.J. Pearce, Supplementary material, 2023, http://dx.doi.org/10.5281/zenodo.8047510.

[95] M.A. Puso, T. Laursen, J. Solberg, A segment-to-segment mortar contact method for quadratic elements and large deformations, Comput. Methods Appl. Mech. Engrg. 197 (2008) 555–566.

[96] K.L. Johnson, Contact Mechanics, Cambridge University Press, 1987.

[97] I. Temizer, A mixed formulation of mortar-based frictionless contact, Comput. Methods Appl. Mech. Engrg. 223 (2012) 173–185.

[98] H. Tada, P.C. Paris, G.R. Irwin, The Stress Analysis of Cracks, Handbook, Vol. 34, Del Research Corporation, 1973.

[99] M. Ainsworth, Essential boundary conditions and multi-point constraints in finite element analysis, Comput. Methods Appl. Mech. Engrg. 190 (2001) 6323–6339.

[100] M. Nejati, A. Paluszny, R.W. Zimmerman, On the use of quarter-point tetrahedral finite elements in linear elastic fracture mechanics, Eng. Fract. Mech. 144 (2015) 194–221.

[101] R.D. Henshell, K.G. Shaw, Crack tip finite elements are unnecessary, Internat. J. Numer. Methods Engrg. 9 (1975) 495–507.

[102] R.S. Barsoum, On the use of isoparametric finite elements in linear fracture mechanics, Internat. J. Numer. Methods Engrg. 10 (1976) 25–37.

[103] I. Athanasiadis, A.G. Shvarts, Łukasz Kaczmarczyk, K. Lewandowski, Z. Ullah, C. Pearce, Corrigendum to "Energy consistent framework for continuously evolving 3D crack propagation", Comput. Methods Appl. Mech. Engrg. 324 (2017) 54–73, http://dx.doi.org/10.5281/zenodo.7004541, Geneva, Switzerland: Zenodo. (2022).

[104] P. Hutchinson, HYB/TOR Seal Ring and Fuel Brick Groove Wall Crack Opening Tests, Technical Report 207204-01/TR/0001 Issue 2, Wood Nuclear Ltd, Walton House, Birchwood Park, Warrington, 2019.

[105] J. Bonet, R.D. Wood, Nonlinear Continuum Mechanics for Finite Element Analysis, second ed., Cambridge University Press, 2008.